Knowledge-based localization of hippocampus in human brain MRI

Mohammad-Reza Siadat[a,*], Hamid Soltanian-Zadeh[a,b], Kost V. Elisevich[c]

[a]*Radiology Image Analysis Laboratory, Department of Diagnostic Radiology, Henry Ford Health System, One Ford Place, Detroit, MI 48202, USA*
[b]*Control and Intelligent Processing Center of Excellence, Elec. and Comp. Eng. Dept., Faculty of Engineering, University of Tehran, Tehran, Iran*
[c]*Department of Neurosurgery, Henry Ford Health System, Detroit, MI 48202, USA*

Abstract

We present a novel and efficient method for localization of human brain structures such as hippocampus. Landmark localization is important for segmentation and registration. This method follows a statistical roadmap, consisting of anatomical landmarks, to reach the desired structures. Using a set of desired and undesired landmarks, identified on a training set, we estimate Gaussian models and determine optimal search areas for desired landmarks. The statistical models form a set of rules to evaluate the extracted landmarks during the search procedure. When applied on 900 MR images of 10 epileptic patients, this method demonstrated an overall success rate of 83%.
© 2007 Elsevier Ltd. All rights reserved.

1. Introduction

The hippocampus is an important structure of the human brain's limbic system. It is strongly believed that this structure has a key role in the learning process and memory. The variations in volume and architecture of the hippocampus on MRI have been observed with some neurological disorders such as schizophrenia, epilepsy, Alzheimer's disease, cognitive impairment, dementia, temporal pole hypometabolism, neurodegenerative diseases, verbal memory performance, emotion processing, posttraumatic stress disorder, traumatic brain injury, organic amnesia, vascular dementia, and mesial temporal sclerosis [1–18]. On the MRI coronal sections, the hippocampus looks like a peninsula of gray matter in white matter and appears in both left and right hemispheres of the brain. On Fig. 1(a) and (b), the left hippocampus is delineated on coronal and sagittal views, respectively. Note that these figures show no distinct boundaries at the medial and anterior limits of the hippocampus, respectively. In 3D, the hippocampus has a sausage-like shape (see Fig. 1(c)). Details of the hippocampus neurophysiology, anatomy and its appearance on MRI are presented in various publications [2,17,19–22].

In many cases, volumetric analysis of the hippocampus from MRI is recommended for human [23] and animal studies [24]. The conventional methods (manual segmentation) require expert operators and they are usually time consuming. In addition, due to the involvement of human operator in the procedure, manual segmentation is not intrinsically reproducible, although this problem can be greatly limited by standardization of the segmentation procedure [25]. These are limiting factors in intra- and more profoundly in inter-institutional quantitative studies. Due to these problems, extraction of quantitative information from MRI is currently done by a limited number of institutions.

Automated procedures are expected to solve the above problems, thereby making it possible for most medical institutions to benefit from quantitative information extracted from MRI. However, segmentation of the hippocampus with conventional methods, e.g., edge tracking, thresholding, or region growing [26] does not produce acceptable results. The reason is that this structure has relatively low contrast, multiple edges, and discontinuous or missing edges on MRI.

The atlas mapping/warping is among the methods that have been widely used for human brain segmentation [27–36]. For relatively small and highly variable structures like the hippocampus, these methods do not usually provide good results due to the imperfections involved in the registration

* Corresponding author. Tel.: +1 313 874 4349; fax: +1 313 874 4494.
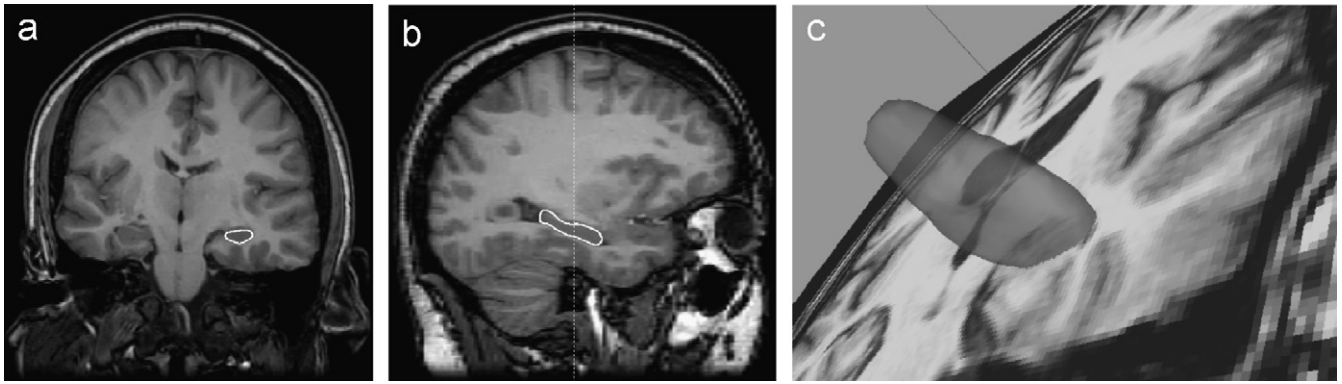 *E-mail address:* siadat@rad.hfh.edu (M.-R. Siadat).

Fig. 1. Hippocampus on T1-weighted images of brain MRI: (a) coronal view with left hippocampus delineated where medial limits show no distinct boundaries; (b) sagittal view with hippocampus delineated where anterior limits show no distinct boundaries; (c) 3D model of hippocampus overlaid on coronal view.

and warping steps. As Hsu et al. [35] reported, reliability of automatic volumetry (using warping method) depends on the selection of the hippocampal template (atlas). Moreover, the warping/mapping methods are computationally inefficient since they deform the entire atlas to match to the entire image data set. In many cases, a single structure (e.g., hippocampus) is of interest, yet the atlas-based methods require warping of the entire brain. Therefore, the conventional atlas warping is neither sufficient nor efficient for localization or segmentation of small structures with high variability in their morphology and location, e.g., hippocampus.

Alternatively, deformable models have been proposed for segmentation of the hippocampus [37–39], and other brain structures from MRI [40,41]. Deformable models treat each structure as a unit object and produce closed boundaries for it. However, all deformable models require an initial state (polygon) from which they start and evolve until they come to a final shape (rest state) [42]. Leaving the definition of the initial polygon to the user may result in low productivity and low reproducibility of the segmentation [43]. Using template (or atlas) mapping/warping to define the initial shape, as proposed in [44–52,38], is insufficient as discussed before. We will utilize a mutual information-based atlas mapping to show how inaccurate this strategy may perform. The inaccuracies in the initialization of small structures like the hippocampus usually result in incorrect segmentation since the edges of neighboring structures can easily absorb the model's boundaries. In the above experiment, we will show how the proposed localization method can guide the atlas-based localization in Section 3. Details of the proposed localization method are described in Section 2. Experimental results and discussions are presented in Section 3. Conclusions and future works are presented in Section 4.

2. Proposed method

The proposed localization method consists of two main steps: (1) information extraction and (2) information analysis, discussed in Sections 2.1 and 2.2, respectively. The information extraction step locates a set of anatomical landmarks on coronal sections of the brain T1-weighted MRI. The information analysis step analyzes the extracted information to determine whether or not the landmarks of the

hippocampus and other structures of interest are accurate and reliable.

The MR images, used in this work, were obtained from epileptic patients using a 1.5 T Signa GE scanner with the following protocol and parameters: 3D IR SPGR, TE = 10 ms, TR = 500 ms, flip angle = 20°, slice thickness = 2 mm, 256 × 256 × 128 voxels, NEX = 2, FOV = 20 cm. The patients contributed in this study are all adult with an age average and standard deviation of 45 and 14 years, respectively.

2.1. Information extraction

When localizing an anatomical structure, especially with low contrast and missing boundaries, the experts tend to look at well-defined and high-contrast neighboring structures to ensure that they have targeted the correct structure. This brings up the notion of making a roadmap to find a desired structure or landmark[1] as final destination. A roadmap consists of a starting point and some milestones with pre-specified road segments guiding a search algorithm from one milestone to the next. A roadmap may require multiple routes to its destination so that it would be possible to evaluate the accuracy and correctness of the final destination.

Unlike the geographical maps, in a brain map the road from one landmark to the next varies among individuals. However, there is an approximate geometrical position for each human brain anatomical structure in which it resides and thus it can be looked for and found. An approximate relative spatial relationship does also exist among the brain anatomical structures. These two postulations make it possible to estimate a set of statistical roads connecting the landmarks of interest: statistical brain roadmap. For hippocampus localization, we estimate the statistical models of the desired and undesired landmarks using the MR images of six patients considered as the training set. This is discussed in Section 2.1.2. The undesired landmarks are located close to the desired ones with similar intensity features to those of the desired landmarks. However, they do not belong to the desired anatomical structures. The desired and undesired models make it possible to balance the sensi-

---

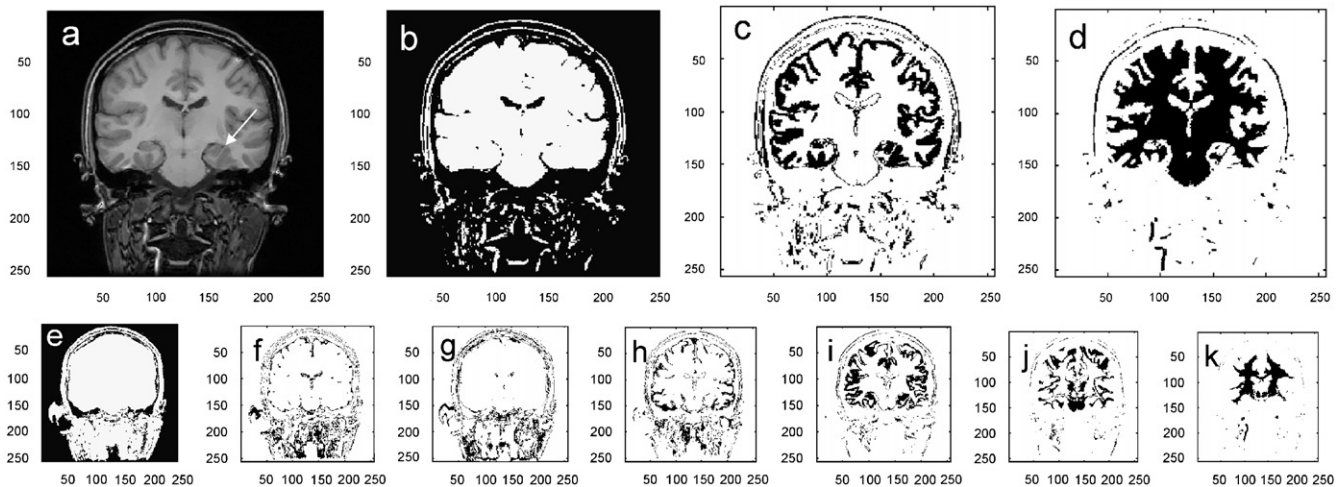[1] In this paper we interchangeably refer to milestones and landmarks.

Fig. 2. Generating binary images using FCM: (a) original image; (b)–(d) binary images representing background and CSF, GM, WM, respectively, generated based on seven clusters produced by FCM, shown in (e)–(k). Note that segmented tissues are shown black in (b)–(k).

tivity (probability of true detection) vs. specificity (one minus the probability of false detection). This leads to the determination of an optimal search area for each desired landmark as the road segment from one milestone to the next. This is discussed in Section 2.1.3. We describe the search algorithm by which the landmarks of interest are searched for and found within the search area in Section 2.1.4. The last two steps will then be applied on our specific application: hippocampus localization, in Section 2.1.5. Since a major part of the proposed algorithm (search method) takes place on binary images of CSF, GM, and WM, we briefly describe how these images are generated in Section 2.1.1.

2.1.1. Generating binary images

We have tested several methods to generate binary images. The examined methods included: (a) histogram analysis (HA); (b) K-Means (KM); (c) fuzzy C-Means (FCM), and (d) iterative self-organizing data analysis (ISODATA) [53–55]. The HA method works based on the assumption that the histogram peaks and valleys can be related to the image background, scalp, muscles, CSF, GM, and WM in a direct, unique and robust way. In real situations, this assumption is not quite reliable. KM and FCM are semi-unsupervised clustering methods in the sense that the user should specify the number of clusters. The ISO-DATA, on the other hand, does not have such a requirement and provides more flexibility. However, working with ISODATA is more complicated (compared to the FCM) due to some required parameter adjustments. The FCM and ISODATA have produced similarly good results for our purpose. We have chosen the FCM since it requires smaller number of parameters. We have used the fcm function offered in the Matlab (Math Works, Boston, MA, USA) Fuzzy Logic Toolbox with default value for the "exponent for the partition matrix U" (i.e., 2.0), maximum number of iterations 200, and minimum amount of improvement 10^{-11}, for seven clusters.

The criteria we use to assess the binary images are focused on the hippocampus region, the insular cortex, and the ventricle structures with an emphasis on the separation of the gray

matter from the white matter and the CSF. For instance, the partial volume effect can result in false connections of the lateral boarders of the hippocampus to the medial point of parahippocampal and fusiform gyri interface (PFGI) or the gray matter at the superior portions of the collateral sulcus. On the other hand, if these separations are over emphasized they may cause false discontinuities within the hippocampus and the insular cortex. Keeping the above trade-off in mind, the collaborating neuro-anatomist assisted us to determine an acceptable combination of the clusters, produced by the FCM with seven clusters. Fig. 2 shows the results of the FCM clustering method (Fig. 2(e)–(k)) and the final three combined binary images (Fig. 2(b)–(d)).

The binary images, which are used in the following sections, are built based on the center of clusters 4–6 (CC4, CC5, and CC6, respectively) when the clusters are increasingly sorted based on their mean values. The three target binary images presenting: (1) background and CSF (Bk&CSF); (2) gray matter (GM), and (3) white matter (WM), are calculated based on the following formulae: $Bk\&CSF < CC4$, $(CC4+(CC5-CC4)/3) < GM < (CC5+7\times(CC6-CC5)/12)$, and $WM > (CC5 + 7 \times (CC6 - CC5)/12)$. One may note that the very tinny GM-WM partial volume strip forming the lateral boundaries of the hippocampus referred to by an arrow on the original image, (Fig. 2(a)). This area is preserved in the GM and WM binary images (Fig. 2(c) and (d)), respectively. The search for the lateral ventricles takes place on the Bk&CSF binary images. These images are also used to find lateral and superior borders of the head to determine the starting point of the roadmap discussed in the following sections. The searches for the rest of the structures are performed on the GM and WM binary images. Note that the above strategy for pre-segmentation of the brain tissues and generating the binary images is neither the best possible method nor is it part of the contributions of this paper. We just used it as an adequate approach to prepare data for the proposed method. Clearly, using more robust and accurate pre-segmentation methods can improve the overall performance.
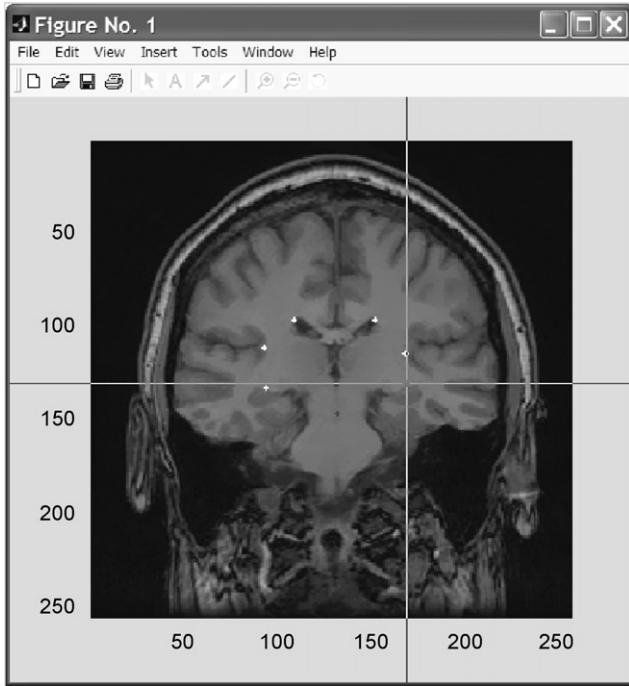
Fig. 3. An instance of marking points of interest: starting points of search: the most lateral points of lateral ventricles, desired points: superior landmarks of hippocampus, undesired points: medial landmarks of insular cortex.

2.1.2. Statistical models of landmarks of interest

To estimate the statistical model for each structure, we have randomly selected six epileptic patients and manually marked the landmarks of interest on over 70 MRI slices. We mark a few undesired structures around each desired landmark to limit the search area and improve the specifi+city. Fig. 3 shows a snapshot of the program by which an expert can browse through MRI slices and mark the desired and undesired points. Using these points, we estimate the statistical models of the desired landmarks as well as those of their neighboring undesired landmarks. The procedure of marking the undesired landmarks is done for each search by taking into consideration all neighboring tissues with similar features as that of the desired point. The undesired landmarks may fall within the search area and possibly mislead the algorithm. Note that the search is performed on the binary images representing the CSF, GM, or WM, so we do not need to consider the neighboring tissues with different intensity characteristics compared to that of the desired structure. After marking the desired and undesired landmarks, a 2D normal (Gaussian) distribution is estimated for each landmark as follows:

$$G(x, y) = \frac{1}{2\pi\sqrt{|\mathrm{Det}(C)|}}$$
$$\times \exp\left(-\frac{1}{2}[x - m_x \; y - m_y]C^{-1}\begin{bmatrix} x - m_x \\ y - m_y \end{bmatrix}\right) \quad (1)$$

where C is the covariance matrix and m_x, m_y are the mean values of the x, and y coordinates of the marked points for each particular landmark. Fig. 4 depicts an instance of the marked landmarks and the summation of their corresponding density functions (when undesired models are considered negative).

2.1.3. Definition of search areas

The search area is usually characterized by a viewpoint, two angles of view, and two far- and near-zone arcs. The viewpoint is usually determined in the initial (rough) roadmap design by an expert, e.g., a neuro-radiologists. To determine the limits of the search area, we first determine a region for each landmark in which it can be most likely found. This region is derived from the statistical model of the structure (shown in Fig. 4(a)) as an iso-contour of the Gaussian model. The volume under the distribution function inside the iso-contour represents the likelihood of residing the landmark inside the region. We call this likelihood "confidence level," as a lower bound at which the detection rate of the search algorithm is set. Finding the iso-contour does not have an analytic solution; so we employ a numerical solution. We use an optimization procedure [56] to calculate the z-value producing the iso-contour for a given confidence level. We set the confidence level at 95% for all structures either desired or undesired throughout this algorithm. The objective function we minimize in this regard is as follows:

$$\mathrm{Obj}(z) = \left| \int\int_{\text{inside iso-contour}(z)} G(x, y)\,\mathrm{d}x\,\mathrm{d}y - 0.95 \right|^2. \quad (2)$$

We use the determined iso-contours and the viewpoint to define the search area. In the simplest case, the view angles are the tangential lines to the desired model's iso-contour from the viewpoint. The search near- and far-zone limits are the tangential arcs to the iso-contour with the viewpoint as their centers. Note that there is greater than 95% probability for the detection of the desired landmark in this search area since it includes more than the area inside the iso-contour. Therefore, in its simplest case, this procedure preserves a lower bound for the confidence level by which the desired structure can be detected. Note that finding the tangential line and arc has straightforward analytic solutions. This search area does sometimes partially cover the iso-contour of a neighboring undesired structure. There are even cases where the desired and undesired iso-contours are intersecting. We take care of these cases by adding limiting lines as described in the example below.

Assume that we would like to determine a search area for the landmarks depicted by pentagram points in Fig. 4(a) from the viewpoint marked by the square point (located at (0 0)). Since there is no undesired structure at the lower-right side of the desired structure, θ_1 can be determined by the tangential line to the iso-contour shown in Fig. 4(a). Also, there is no undesired structure between the viewpoint and the desired structure, so we choose the tangential arc with radius r_1, as the near-zone limit. For the other view angle (θ_2), the iso-contours of the desired and undesired structures (pentagram and circles, respectively) are
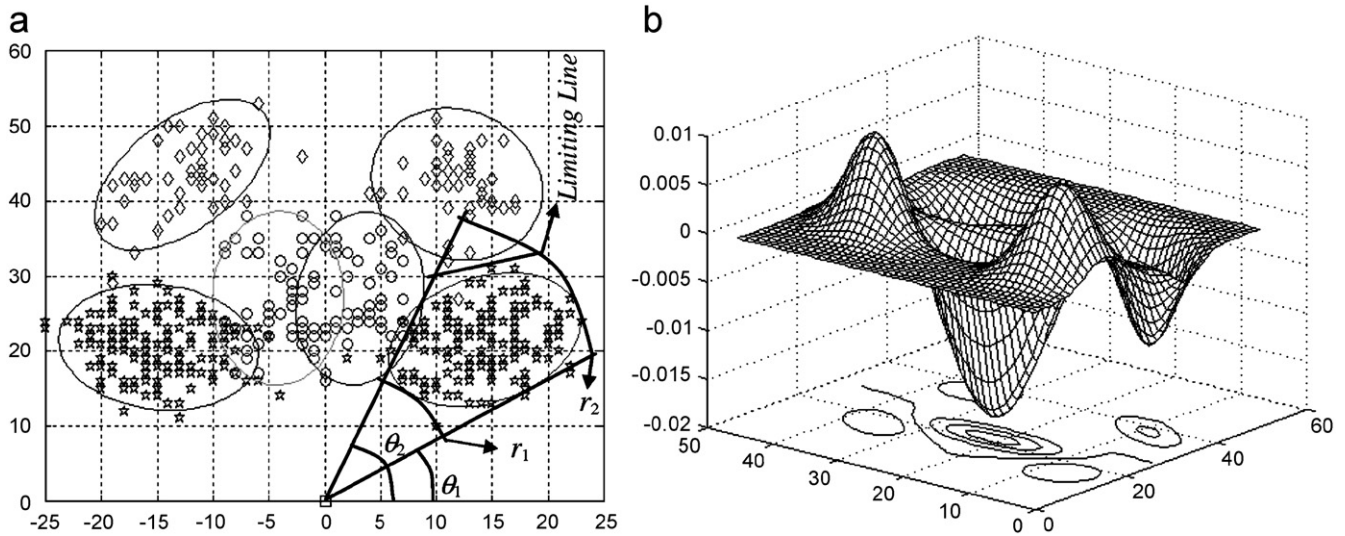
Fig. 4. Marked landmarks and their estimated distributions for an example of six landmarks: (a) marked points with iso-countors drawn where only 5% of volume under estimated distribution function left outside; (b) 3D plot of sum of estimated Gaussian distributions where undesired models are considered to be negative.
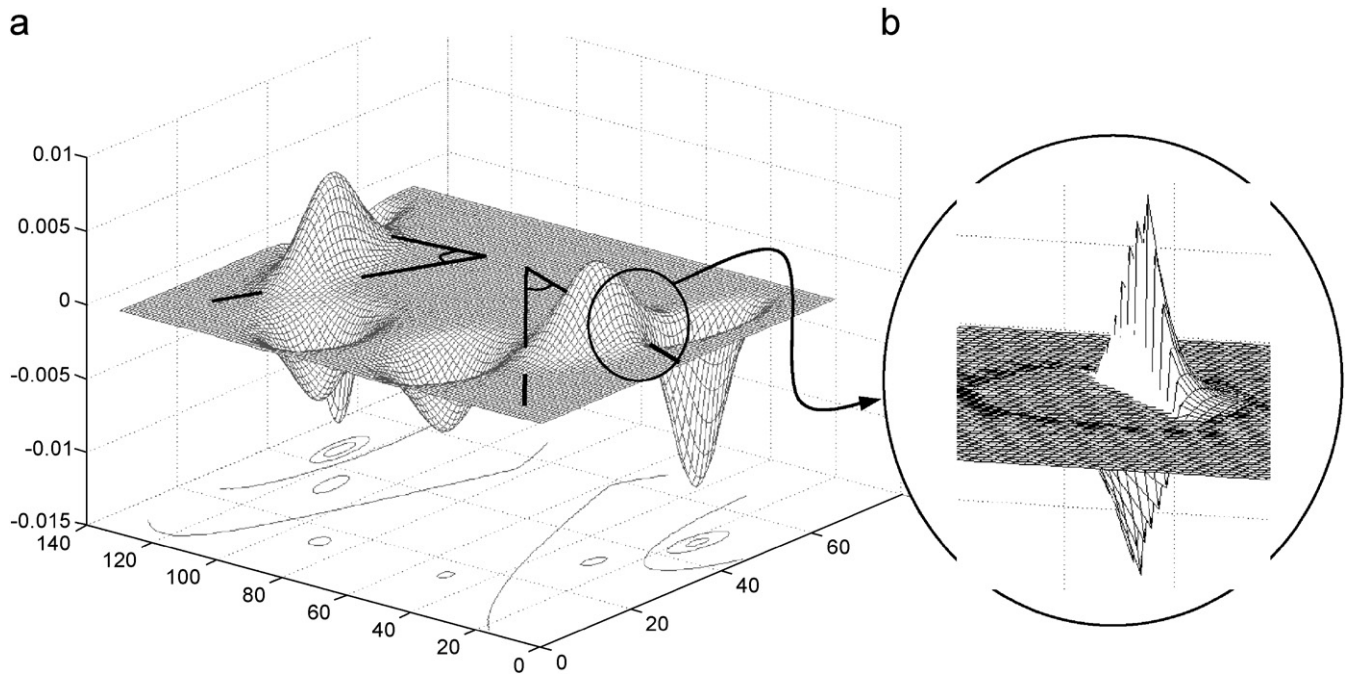

Fig. 5. (a) Illustration of probability density functions (pdf) for six landmarks. pdf's of desired landmarks are shown positive and those of undesired landmarks are shown negative. Black lines show the search angles. (b) Zoomed-in view of the pdf's intersecting with a search boundary.

intersecting. In such cases the "tangential line" solution leads the algorithm to a low specificity, i.e., large number of false alarms, which is not desirable. We propose an optimal solution in the sense that the specificity and sensitivity are balanced. Note that this is an optimal solution only if there is no tendency toward finding the desired structure at the cost of getting more erroneous landmarks (higher false alarm) or preventing false alarms at the cost of lower detection rate.

Fig. 5(a) shows a 3D illustration of an overall distribution map made up of the sum of all the probability density func-

tions where undesired models are considered to be negative. Note that this overall map is not a probability density function. Fig. 5(b) shows portions of the desired and undesired density functions outside and inside of the search angle, respectively, as positive and negative edges. The positive edge corresponds to the probability of missing the desired structure (1-sensitivity). The negative edge corresponds to the probability of false alarm (1-specificity). The specificity and sensitivity are balanced when the volume of the positive and the negative portions shown in Fig. 5(b) are equal. Therefore, we minimize
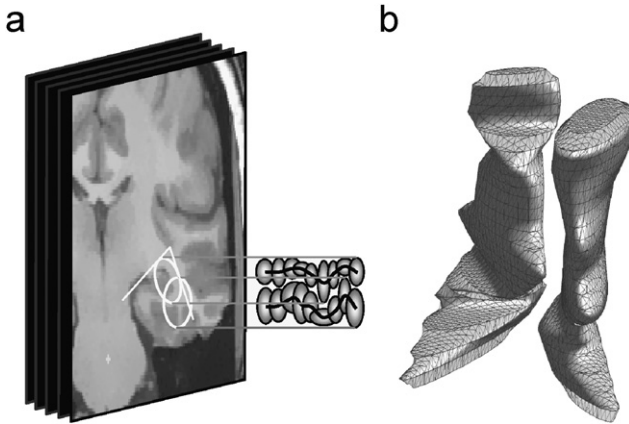
Fig. 6. (a) Schematic showing a case where distributions of landmarks on each individual slice/location are completely separate while their projections on 2D space overlap. (b) An actual case illustration in which 3D iso-surface of desired and undesired landmarks are separate while their 2D projections overlap.

the objective function in formula (3) to obtain this optimal solution

$$\text{Obj}(\theta) = \left| \int\int_{\text{search angle side}} G_u(x, y)\, dx\, dy \right.$$
$$\left. + \int\int_{\text{outside the search angle}} G_d(x, y)\, dx\, dy \right|^2,$$
(3)

where G_d and G_u are the desired and undesired models, respectively, and θ is the angle of view (θ_2 in Fig. 4(a)). The positive and negative portions shown in Fig. 5(b) correspond to the first and the second terms in (3), respectively.

There are cases in which the desired and undesired distributions are (partially) at the same angle of view and the search area contains part of the undesired models. Fig. 4(a) shows an instance of such case for the far-zone limits where the pentagrams represent the desired and the diamonds represent the undesired structures. In this case, we estimate a limiting line (Fig. 4(a)) in addition to the tangential arc. Then we define the search limit at each angle by the one that is closer (farther for near-zone limits) to the viewpoint (see Fig. 4(a)). To estimate the limiting line, we consider the volumes under the undesired and desired density functions inside the search area and on the other side of the limiting line, respectively. We move the line to minimize the difference between these two volumes. Since such an optimal line does not usually pass through the viewpoint (origin of the coordinate system), we estimate the intercept of the line in addition to its slope. So an objective function of two parameters is optimized, $\text{Obj}(\theta, h)$, where h is the intercept of the limiting line.

There are cases in which the 2D density functions highly overlap and the theoretical error (false alarms and missing landmarks) are higher than the actual error. We explain the reason using the schematic shown in Fig. 6(a) and an actual 3D illustration shown in Fig. 6(b). By projecting the marked points

acquired in 3D space into the 2D space and building the 2D statistical models, we assume that the landmarks of interest have a co-centered distribution in the third dimension. Given the fact that the points are marked in a very thin portion of the image space (20–30 mm thick) this assumption is often valid. However, there are occasional cases in which the distributions of a landmark are not co-centered in the third dimension. So while the landmarks' models highly overlap on their 2D projection, they are separated in their 3D distribution (Fig. 6(b)). This observation leads us to a very important fact that constitutes our search method. The fact is that the proposed search method mimics the mechanism by which light rays come into the eyes of an observer (see Section 2.1.4). The closer object is seen first no matter how overlapped its 2D projection is with that of the other objects in the scene. Keeping the above observation in mind and looking at Fig. 6(a) one can easily see that the proposed search makes it impossible to reach the undesired structures' iso-contours before passing the iso-contours of the desired structure. In fact there is no intersection when the 3D models of the structures are considered (Fig. 6(b)).

Up to this point, we have assumed a fixed viewpoint (usually a previously found anatomical landmark) from which the search is initiated. We can relax this criterion and look for a better viewpoint. This is what we have done to adjust the viewpoint of the search from the lateral ventricles for the superior landmarks of the hippocampus. We will go into the details of this experiment in Appendix A.2. In such cases, the objective function is very similar to (3) with the extra step of intercept estimation, i.e., $\text{Obj}(\theta, h)$. The only difference is that we find all the optimal limiting lines between each pair of desired–undesired distributions and then decide which pair of lines provide a close intersection to the original viewpoint and thus should be considered as the angles of view. Since we use at most the four closest undesired structures around the desired one, there remain at most two other lines that determine the far- and near-zone limits of the search if they make a smaller search area compared to the tangential lines/arcs drawn based on the new viewpoint. In cases with less than four undesired structures, we choose the missing limit by fitting a tangential arc/line to the iso-contour. Note that we do not change the viewpoint radically since it puts a strong bias on the selection of the surrounding undesired points and the process of manual landmark identification on the training set. In our experiment with the hippocampus, there is one actual case (search from superior landmark of the hippocampus for its inferior landmark) with the same situation (suggesting a radical viewpoint movement) that we will discuss in details in Appendix A.5.

2.1.4. Search method (traversing search area)

In general, the search is performed from an initial boundary (also referred to as distance or radius) relative to a viewpoint and expands toward a final boundary (r_1 and r_2, respectively, in Fig. 7(a)). For each radius all the pixels between two angles of view (θ_1 and θ_2 in Fig. 7(a)) are examined to find a structure with a specific condition on its color (black or white on the binary images) and/or spatial connectivity before decreasing
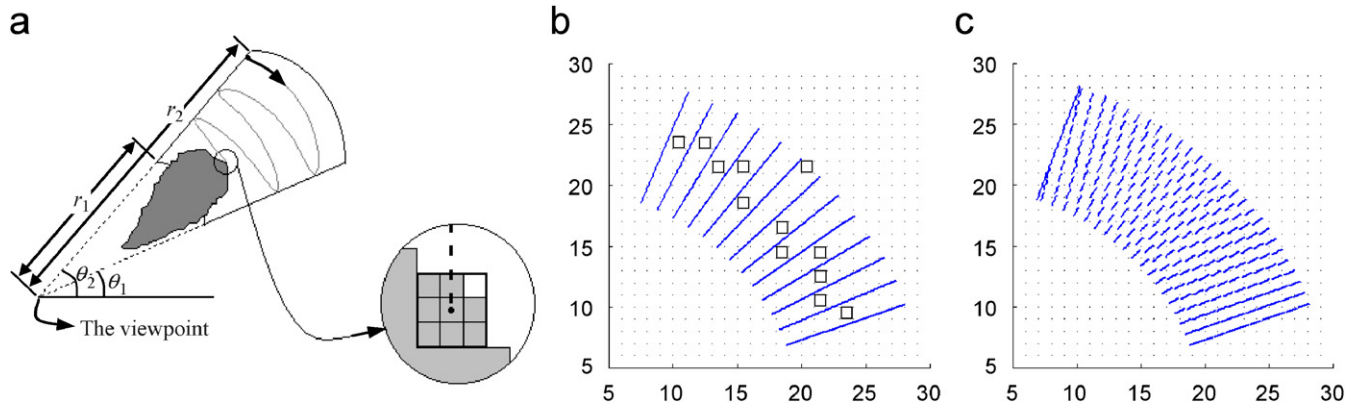
Fig. 7. (a) Search method mimicking emission of radii of sight; (b) fixed angle step-size and possibility of missing pixels while traversing search area. Squares present some of missing pixels; (c) determining angle step-size adaptively leaves no pixel untouched/unexamined.
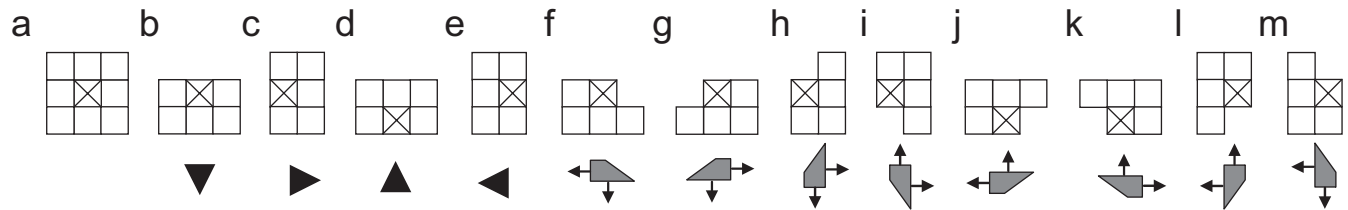

Fig. 8. Structuring elements of finding connected components (FCC) algorithm modified to grow directionally.

or increasing the search radius. When the smaller boundary is the initial one, this search method looks very similar to the way light traverses the space when departing a point source. When the initial boundary is the larger one, it is similar to the way light rays travel into the eyes of an observer. In the simplest case, the search looks for a pixel with a particular "color." To decrease the sensitivity to the image noise, we may search for a pixel with specific spatial connectivity constraint (e.g., 8-neighbor connectivity). For example, in Fig. 7(a) a dark point with at least 7 dark neighbors in an 8-nearest neighborhood is searched for and found. Once a point satisfies the search condition, an enhanced morphological algorithm based on finding connected component (FCC) [57] is invoked. Using one of the structuring elements shown in Fig. 8 FCC is used to grow the connected regions (in a specific direction) and eventually reach to a superior, inferior, lateral, or medial landmark.

To ensure all of the pixels in a search region are viewed, we determine the angle step-size as a function of the radius. The worse case scenario occurs for the pixels with sides perpendicular to the direction of the view angle (light ray). Therefore, the angle step-size should be smaller than the angle introduced by the pixel-side segment and the coordinates of the viewpoint, i.e., $\Delta\theta \leqslant \arctan(1/r)$ where r is the length of the segment connecting the viewpoint to the examined point. A search with a fixed angle step-size either leads to inefficiency (each pixel is examined more than one time) or fails to examine all the pixels (in Fig. 7(b) unexamined pixels are marked with squares). Unlike the case with a fixed angle step-size, the adaptive

method (Fig. 7(c)) proposed here provides a relatively efficient search and guarantees to examine all the pixels in the search area.

2.1.5. Application of proposed method to hippocampus

The anatomical structures of interest participating in the roadmap include the lateral ventricles, insular cortex, and hippocampus. The proposed search approach finds the lateral ventricles on the CSF binary images from the starting point of the roadmap. Note that the roadmap's starting point (Fig. 9, point-1) is located on the brain midplane inferior to the most superior point of the head by half of the head width. The FCC algorithm is utilized to extract the whole ventricle structure and locate its particular landmarks. Using the lateral landmarks of the lateral ventricles, we initiate a search to identify a landmark on the superior borders of the hippocampi (Fig. 9, point-2). From this landmark, search regions are defined to identify the medial inferior landmark of the hippocampus and the insular cortex (Fig. 9, point-3 and point-4, respectively). The medial inferior landmarks of the insular cortex are located using the FCC algorithm. These landmarks define search regions to identify lateral landmarks of the hippocampi. Using the lateral and the inferior points of the hippocampus a search from the superior landmark of this structure is performed to find a fourth point (somewhere between the lateral and inferior points) of this structure. The searches for the superior and the lateral landmarks of the hippocampus and the insular cortex take place on GM binary images. The search for the inferior and the fourth point of the hippocampus is performed on WM binary images.

Details of the statistical models and search areas for the above roadmap and its milestones are presented in Appendix A.

2.2. Information analysis

At this step, we evaluate the reliability of each slice-landmark generated during previous step: information extraction. We employ several rules as the knowledge-based core of the proposed system to distinguish the inaccurate or inappropriate landmarks
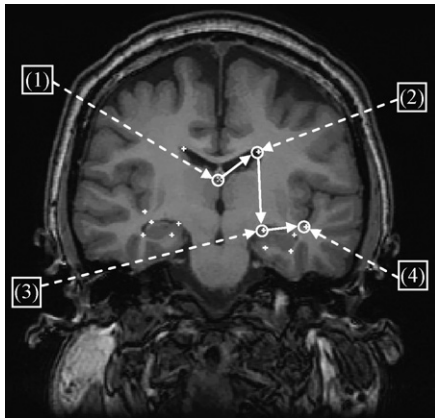

Fig. 9. Milestones of roadmap to localize left hippocampus: (1) starting point of roadmap; (2) most lateral landmark of left lateral ventricle; (3) a point on superior limits of left hippocampus, and (4) most inferior-medial point of left insular cortex. Solid arrows show the sequence in which milestones are visited.

found during the information extraction (Section 2.1). The proposed rule-based system acts as an intelligent filter in ruling out the inappropriate landmarks and corresponding slices. The approach to design the rules using the estimated statistical models is presented in Section 2.2.1. The approximate reasoning proposed to combine the results of the rules is discussed in Section 2.2.2.

2.2.1. Proposed rules

We have defined 14 rules for the proposed knowledge-based system. Each rule generates an intermediate confidence factor (ICNF). An ICNF is usually determined based on a particular abstract concept associated with the high-level object(s). We have defined three categories of rules based on: (i) absolute location of the landmarks; (ii) relative locations of the landmarks compared to each other; and (iii) general symmetry of the brain.

The first category is based on our first postulation that the brain structures and landmarks have ballpark locations on the slices with hippocampus across a generation of normal cases or epileptic patients and that this ballpark can be statistically modeled. The same training set as that of Section 2.1 has been used for estimation of the absolute statistical models. Fig. 10(a) depicts the marked points and the iso-contours of the models estimated for the desired landmarks. The iso-contours are determined at 95% confidence level. This guarantees the probability of detection (sensitivity) of the associated rules to be at least 95%. The models shown in Fig. 10(a) demonstrate the absolute locations of the landmarks of interest in a coordinate system with the first point of the roadmap as its origin. If a landmark is found in an unexpected region, the confidence
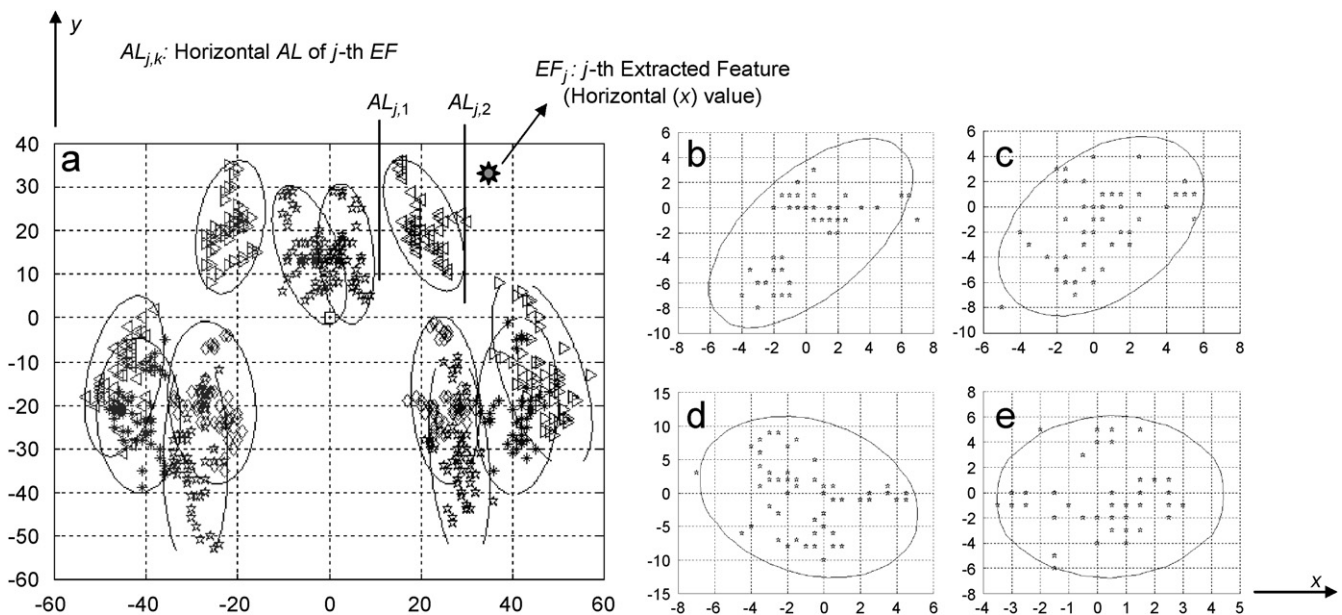
Fig. 10. (a) Absolute coordinates of lateral and medial points of lateral ventricles (pentagrams and triangles, respectively), superior, lateral, and inferior points of hippocampus (diamonds, stars, and pentagrams, respectively), and medial inferior points of insular cortex (triangles). All points are given in a coordinate system built on starting point of roadmap (define in Section 2.1) as origin. The iso-contours are drawn at 95% confidence level. (b)–(e) Deviations in y-coordinate for each pair of a landmark in left and right hemisphere vs. deviation of average of corresponding x-coordinates from brain midline, (b) lateral, (c) inferior landmarks of hippocampus, (d) medial inferior points of insular cortex, (e) lateral landmarks of lateral ventricles.

of the system in correct identification of the landmark decreases. For instance, a point found as the superior landmark of the hippocampus with a vertical (y-) coordinate greater than zero or less than −36 (almost 30 mm) is not supported by the absolute location distribution of this landmark (diamonds in Fig. 10(a)). The above distribution also introduces horizontally acceptable limits (AL) in which the superior points of the left and right hippocampi may fall. An absolute rule checks all AL for an extracted point and generates an ICNF depending on how well the extracted features (EF) of the point (e.g., horizontal or vertical coordinates) match the ALs. When all ALs of a rule are satisfied, a maximum ICNF score of 100 is generated that strongly supports the extracted point. The minimum ICNF score is zero that strongly denies an extracted point to be a representative of the corresponding landmark. When the EFs of the extracted point do not satisfy some or all ALs, the rule performs a soft transition from its absolute supportive state (ICNF = 100) to its absolute denial state (ICNF = 0) based on formula (4),

$$ICNF_i = \begin{cases} 100 - \alpha_i, & \alpha_i < 100, \\ 0, & \alpha_i > 100, \end{cases} \qquad (4)$$

where

$$\alpha_i = \left(\sum_{\text{features of the } i\text{th rule}} (TP_{i,j} \times \min_k(EF_j - AL_{j,k}))^2 \right)^{0.5} \qquad (5)$$

and $TP_{i,j}$ is the softening parameter that governs the transition of the i-th rule based on an unacceptable mismatch in jth AL, and EF. TP is usually set to 7.8 in our work extending the transient strip to 7.8 mm. When AL has more than one limit (e.g., min and max limits for the vertical location of the superior landmarks of the hippocampus), formula (5) uses the limit, which is closer to the extracted feature (e.g., shortest distance from the acceptable region). We have absolute rules for each landmark of interest introduced in Fig. 10(a) except for the most medial points of the lateral ventricles. We did not design an absolute rule for this landmark since there are cases in which the third ventricle is connected to the lateral ventricles in 2D view and as a result the most medial points of the lateral ventricles are not reliable for an absolute location testimony. Thus, we have five absolute rules in the proposed rule-based system.

The second category of the rules is based on our second postulation indicating that approximate relative spatial relationships exist among the brain anatomical structures. So, one particular landmark is expected to be superior, inferior, interior, or lateral compared to another landmark. These qualitative expectations are converted to quantitative relations based on the statistical models shown in Fig. 10 as well as the ones derived in the information extraction section.

As an example, we explain the details of the design for a relative rule that quantitates the following qualitative rule: "the superior and lateral landmarks of the hippocampus should not have significantly different vertical coordinates (i.e., along the y-axis)." The absolute statistical models shown in Fig. 10(a) (diamonds and star models) suggest that the linguistics label "not significantly different in vertical coordinates" to be as
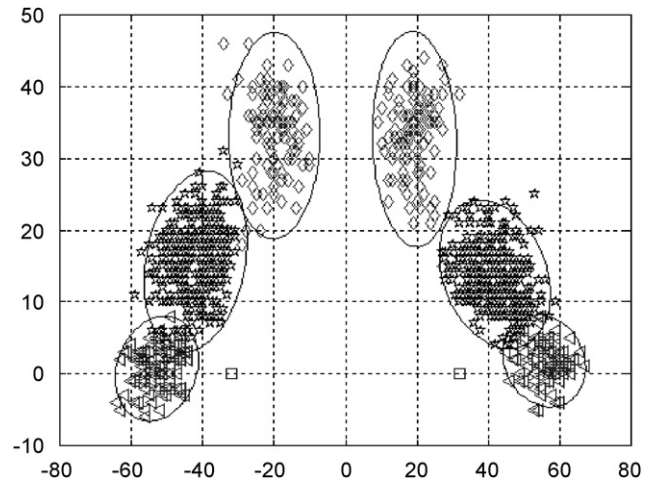

Fig. 11. Distribution of medial inferior landmarks of insular cortex shown as pentagram in coordinates system built on superior landmarks of hippocampus as origin.

much as 31.2 mm (about 40 pixels in this example) for this case. However, further investigations show a lower bound for this term. We will explain this in details in the following paragraph.

Considering the model estimated in Appendix A.3 for the medial inferior points of the insular cortex (Fig. 11 pentagram points) in the superior points of the hippocampus coordinates (Fig. 11 square points), we can estimate a distribution model for the superior points of the hippocampus in the insular cortex coordinates. This model would be the same as its counterpart only with the difference of being centrically projected around the middle of the segment connecting the mean value of the insular cortex model and the origin, i.e., superior point of the hippocampus. Keeping this point in mind and looking at Fig. 11, we have applied the centric-projection and found out that the superior point of the hippocampus is stretched somewhere from 3.9 to 19.5 mm in y-axis (about 5 to 25 pixels) underneath the insular cortex based on the iso-contour of 95% confidence level. On the other hand, the model estimated for the lateral point of the hippocampus from the medial inferior point of the insular cortex in Appendix A.4 shows that the lateral point of the hippocampus is distributed from 2.3 to 11.7 mm (about 3–15 pixels) underneath the insular cortex. These two observations suggest the use of 17.2 mm (about 22 pixels) as a maximum AL to describe the term "not significantly different," in this case. The underlying rationale based on which we can set a lower bound for this case is the fact that using the models estimated in Appendix A.3 and A.4, eliminates the uncertainty brought in by the roadmap's starting point to the absolute models shown in Fig. 10(a). The rules in this category follow formula (4) on their transition from absolute supportive state to absolute denial state.

We have designed relative spatial rules to examine the spatial relationships of: (a) the lateral and interior landmarks of the lateral ventricles, (b) superior and inferior points of the hippocampus, (c) the superior point of the hippocampus and interior/inferior point of the insular cortex. There are other possible

combinations of landmark pairs for which a relative rule could be designed. However, such pairs are linearly dependent to the rules we have just proposed. As an example there is no need to examine the relationship of the insular cortex and the lateral landmark of the hippocampus since it is not independent of the rule discussed in previous paragraph and (c). Although the interior points of the lateral ventricles are not reliable, as mentioned before, we are proposing in (a) a relative rule in which this landmark is participating. As pointed out previously, the reason for the interior point to be "unreliable" is that sometimes, in 2D views, the third ventricle is connected to the lateral ventricles. This may pull down the interior points unpredictably. Therefore, even though the lower limits of this structure is not reliable we can still set a limit on its upper bound relative to the lateral points of the lateral ventricles. The corresponding rule verifies the upper part of the lateral ventricles to have a 'V' shape.

The third category of the rules is based on general symmetry of the brain. If MR images are acquired in the coronal or axial directions/cross sections (oror a combination of these two directions), the symmetry feature will be observed with respect to the midplane. The symmetric rules are designed based on the statistical models derived here and partially shown in Fig. 10(b)–(e). It is expected that the corresponding landmarks at left and right hemispheres satisfy the following conditions: (1) the horizontal (x-) coordinates average around brain midline; (2) the vertical (y-) coordinates are not significantly different. We assume that the roadmap's starting point is on the brain midplane, therefore, the "x-coordinates averages of the symmetrically located landmarks" are supposed to be around the x-coordinate of the roadmap's starting point.

The term "not significantly different" is interpreted for each case based on the statistical models (partially) shown in Fig. 10(b)–(e). For instance for the inferior points of the hippocampus the corresponding model, the iso-contour in Fig. 10(c), suggests that the left and right landmarks may be at most 7 mm (about 9 pixels) apart in their y-coordinate. For the deviation of the horizontal average from the roadmap's starting point, it is expected to be no more than 4.7 mm (6 pixels). There are four rules similar to the one explained above for (a) the superior and (b) lateral landmarks of the hippocampus; (c) the lateral points of the lateral ventricles, and (d) the medial inferior landmarks of the insular cortex. The symmetric rules follow formula (4) on their transition from absolute supportive state to absolute denial state.

2.2.2. CNF calculation

The sample mean of the intermediate confidence factors, IC-NFs, is used to compute the overall confidence factor, CNF. The rationale for computing the sample mean is that each ICNF can be considered as an estimate of the probability of the slice containing the hippocampus, and thus each ICNF is a random variable. For independent ICNFs, the sample mean generates the minimum variance estimate of CNF. If CNF is greater than a pre-specified threshold, the slice is determined to contain the hippocampus. In addition, the landmarks found around the hip-

pocampus are assessed to be accurate enough and therefore, valid. In this study, the threshold is set to 90 while CNF range is from 0 to 100. The average and standard deviation of CNF for slices without hippocampus for the training set are 40.15 and 15.01, respectively.

We have selected the threshold conservatively to ensure no wrong or inaccurate landmarks are considered as valid, since such an error, depending on its severity, may cause a problem for the next step of the segmentation (i.e., deformable model). The underlying assumption is that applying the proposed search method on slices without hippocampus either produces no results or the results are randomly distributed such that the above rules will always detect and filter them out. On the other hand, the slices with the hippocampus produce points that are scored above the threshold by the rules.

3. Experimental results and discussion

We apply the proposed method to the MR images of 10 randomly selected temporal lobe epileptic patients and evaluate its performance. Fig. 12 illustrates sample results of the hippocampus initialization (first row) and the corresponding final segmentations provided by the deformable model (second row) in sagittal and coronal views. Details of the 3D deformable model used in our experiments are presented in [58,59]. Quantitatively, we first assess the success of the first phase of the algorithm, the information extraction, during which the landmarks of interest are found. Then we present the assessment of the information analysis phase during which the landmarks are evaluated. Finally, the overall evaluation of the proposed method including the final step, deformable model segmentation, is reported.

If a point is accurately found on a slice with the landmark of interest (e.g., hippocampus) or no point is found on the slices without the landmark of interest, then it is considered a success, for the information extraction phase. If a point is found on a slice with no landmark of interest, or the point is not accurately found where the landmark of interest exists, then it is considered a failure. The success rates of the information extraction phase for each individual patient and in overall are presented in Table 1.

For the information analysis phase, we consider two measures by which the performance of this phase is assessed: specificity and sensitivity. We calculate the specificity as the ratio of the number of slices with CNF < 90 over the number of the slices without hippocampus or with the landmarks of interest inaccurately found. The sensitivity of the information analysis phase is defined as the ratio of the number of the slices with CNF $\geqslant$ 90 over the number of slices the landmarks of interest are all accurately found. The first two rows of Table 2 summarize the above definitions. For these two measures we have obtained very high overall scores of 99.50% (STD: 1.58%) and 98.89% (STD: 3.51%), respectively. This indicates that the proposed rule-based system has performed very well. The scores for different patients are reported in the "information analysis" columns of Table 1.
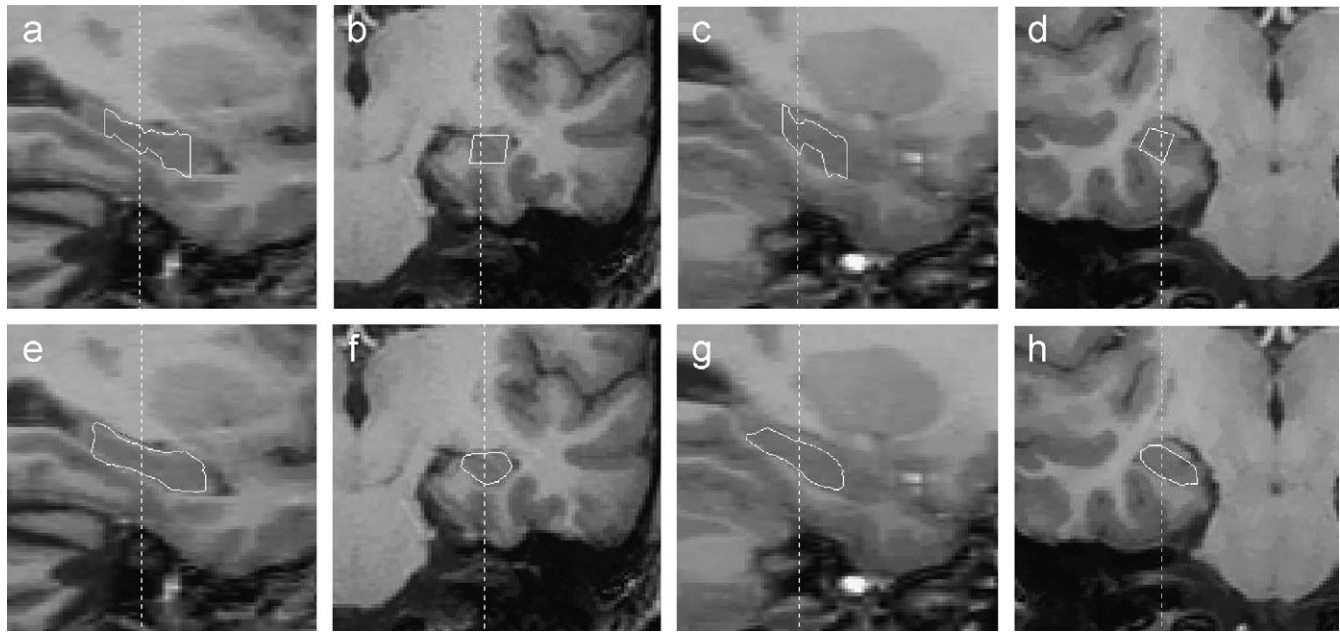
Fig. 12. (a)–(d) Sagittal and coronal pairs of T1-weighted MRIs of two subjects with initial contours overlaid. (e)–(h) Sagittal and coronal pairs of T1-weighted MRIs with the final contours overlaid.

Table 1
Results of proposed algorithm for information extraction and analysis steps and overall system

Patient no.	Information extraction	Information analysis		Accuracy	Overall sensitivity	Overall success rate
		Specificity	Sensitivity			
1	78.67	100	100	99.17	66.67	80.00
2	71.67	100	100	100.0	91.67	95.00
3	70.63	100	100	99.07	75.00	85.71
4	90.10	100	100	98.48	78.57	81.25
5	71.25	100	100	100.0	66.67	80.00
6	55.75	100	100	100.0	60.00	86.21
7	64.77	100	100	100.0	54.55	77.27
8	66.67	100	100	99.07	75.00	85.00
9	58.97	95	100	95.83	54.55	80.77
10	62.88	100	88.89	100.0	66.67	81.82
Average	69.14	99.50	98.89	99.16	68.94	83.30
Standard deviation	9.95	1.58	3.51	1.30	11.51	5.00

We consider the "accuracy" of the algorithm as the number of the accurate points found for the landmarks of interest divided by the total number of the points found for the landmarks of interest on all slices with and without the hippocampus with CNF $\geqslant$ 90 (third row of Table 2). Note that in our experiments, there is no circumstance under which the CNF $\geqslant$ 90 for slices without the hippocampus. The mean, the standard deviation, and the maximum CNF for the slices without the hippocampus are 30.75, 19.66, and 87.5, respectively. The accuracy is important since the points evaluated to be "accurate" will define the hippocampus initial polygon as the final product of the proposed localization method. The outstanding total accuracy of 99.16% with a minimum of 95.83% is far beyond the deformable model demands. There were 8 inaccurate points throughout this experiment where the initial models have 1008

points in total. The inaccuracies mostly caused by the fourth point of the hippocampus (7 out of 8 inaccurate points). Note that we did not estimate a model and there is no rule to examine the fourth point's accuracy in the information analysis phase. This means that the proposed statistical models and evaluation methods failed only once in 1008 cases. The results for different patients are reported in the "accuracy" column of Table 1.

The proposed method did not generate any false alarms (defined in the fifth row of Table 2). Thus, we do not report it in Table 1. The next measure is the "sensitivity," which is the number of detected slices with an accurately identified hippocampus and a CNF $\geqslant$ 90 divided by the total number of slices with the hippocampus (fourth row of Table 2). The scores are listed for each patient in Table 1. The "overall sensitivity" is 68.94% (STD: 11.51) considering all patients.

Table 2
Summary of definitions of measures by which we have evaluated performance of proposed method

	CNF ⩾ 90	CNF < 90	Descriptions
Accurate landmarks on slices with hippocampus	■		Information analysis sensitivity: (no. of slices with CNF ⩾ 90)÷(no. of slices with landmarks of interest accurately found)
Inaccurate landmarks on slices without hippocampus		■	Information analysis specificity: (no. of slices with CNF < 90)÷(no. of slices without the hippocampus or with the landmarks of interest inaccurately found)
Slices with and without hippocampus	■		Overall accuracy: (no. of accurate points)÷(total no. of points on slices with CNF ⩾ 90)
Slice with hippocampus	■		Overall sensitivity: (no. of slices with hippocampus & CNF ⩾ 90)÷(no. of slices with hippocampus)
Slice without hippocampus	■		Overall false alarm: (no. of slices with CNF ⩾ 90)÷(no. of slices without hippocampus)
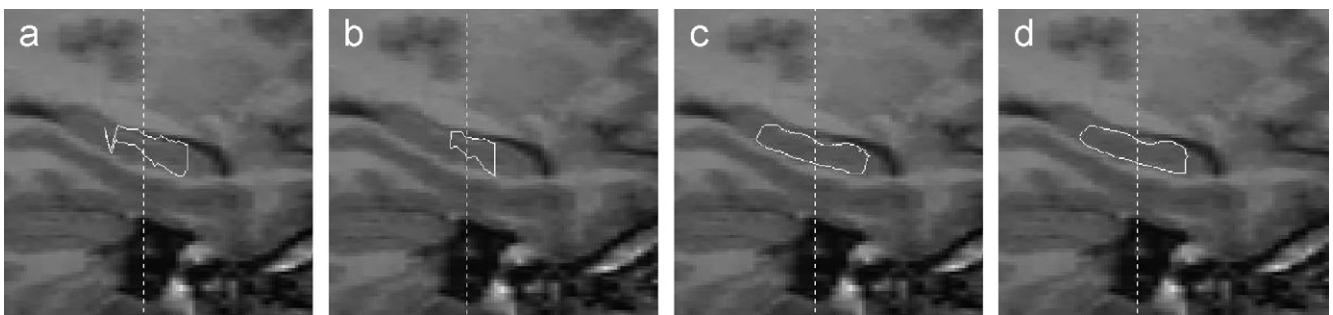
Fig. 13. Sagittal cross sections of the hippocampus with initial polygons produced using two different sensitivity levels for initialization: (a) 78% (b) 41%. The final segmentation results (c) and (d) produced by deformable model using initial models shown in (a) and (b), respectively. Note robustness of proposed method.

It is extremely important to note that our deformable model can easily perform under even a much lower sensitivity. To show this, we have randomly removed some of the initial point-slices from the original initialization results (Fig. 13(a)), to decrease the sensitivity to 41.67% (5 point-slices out of 12 for one of the patients) (Fig. 13(b)). We have then applied the deformable model on the original and the reduced initial models. The differences in the final segmentations were evaluated with visual inspection and a similarity measure. The visual inspection resulted in very good correspondences as shown in Fig. 13(c),(d). The similarity is defined as:

$$\text{similarity} = \frac{1}{n} \sum_{i=1}^{n} \frac{\#(\text{SegOrg}_i \cap \text{SegRd}_i)}{\#(\text{SegOrg}_i \cup \text{SegRd}_i)},$$

where SegOrg_i and SegRd_i are the segmented hippocampus on the ith slice estimated based on the original and reduced initial models, respectively. The function $\#(A)$ returns the cardinality of set A. The similarity measure of the left hippocampus for the above case is 0.83, the average distance of the two surfaces is 0.57 mm, and the volume correspondence is 90.10%. Therefore, the sensitivity provided by the proposed initialization method is well beyond the demands of the deformable model.

The final measure is the overall success rate of the algorithm in performing its ultimate goal: localization of the hippocampus. This measure is calculated as the ratio of the

number of correct decisions made by the knowledge-based system divided by the total number of slices introduced to it. A correct decision is producing a CNF ⩾ 90 when the introduced slice contains the hippocampus structure or producing a CNF < 90 when there is no hippocampus. The overall success rate of the proposed algorithm is 83.30% (STD: 5.0%).

Table 3 presents the average boundary distances and the similarity measure of the initial and automatic (final) segmented models compared to the neuro-anatomist manual segmentation for each patient and for each side, separately. The overall average distances of the initial models (polygons) are 2.21 and 2.01 mm with standard deviations of 0.32 and 0.24 for the left and right hippocampi, respectively. The overall average distances of final segmented models are 1.80 and 1.70 mm with standard deviations of 0.42 and 0.47 for the left and right hippocampi, respectively. The overall similarities of the initial models are 0.49 and 0.56 with standard deviations of 0.07 and 0.09 for the left and right hippocampi, respectively. The overall similarities of the final segmented models are 0.63 and 0.64 with a standard deviation of 0.07 and 0.05 for the left and right hippocampi, respectively. The volume correspondences of the final segmented models and the manual ones are 57.97% and 62.05% with standard deviations of 14.59% and 13.85% for the left and right hippocampi, respectively.

Table 3
Average boundary distance, overlap similarity, and volume correspondence measures for initial and final segmented models in comparison with manual segmentation

Patient no	Initial models average distance, left hemisphere (mm)	Final models average distance, left hemisphere (mm)	Initial models average similarity (left)	Final models average similarity (left)	Final models volume correspondence (left) (%)	Initial models average distance, right hemisphere (mm)	Final models average distance, right hemisphere (mm)	Initial models average similarity (right)	Final models average similarity (right)	Final models volume correspondence (right) (%)
1	1.74	1.68	0.5697	0.6415	55.83	1.94	1.40	0.6043	0.6771	63.82
2	2.14	1.25	0.4422	0.7603	63.80	1.96	1.52	0.5534	0.6761	61.43
3	1.92	1.95	0.5028	0.5767	29.73	2.30	1.80	0.4277	0.5879	30.86
4	1.87	1.60	0.5289	0.6109	44.92	2.09	1.69	0.5042	0.5909	55.95
5	2.21	1.84	0.5138	0.5616	54.74	2.03	2.81	0.5894	0.5500	53.22
6	2.76	2.14	0.4501	0.5949	54.39	1.94	1.93	0.6026	0.6630	80.28
7	2.12	1.36	0.5868	0.7300	68.52	1.55	1.16	0.6727	0.6996	73.50
8	2.56	1.79	0.4181	0.6135	61.66	2.40	1.17	0.4076	0.6643	70.14
9	2.47	2.72	0.3533	0.5977	60.66	1.80	1.72	0.5590	0.6351	71.96
10	2.32	1.69	0.4929	0.5811	85.42	2.07	1.81	0.5919	0.6451	59.33
Average	2.21	1.80	0.4859	0.6268	57.97	2.01	1.70	0.5565	0.6389	62.05
Standard deviation	0.32	0.42	0.0711	0.0665	14.59	0.24	0.47	0.0859	0.0479	13.85
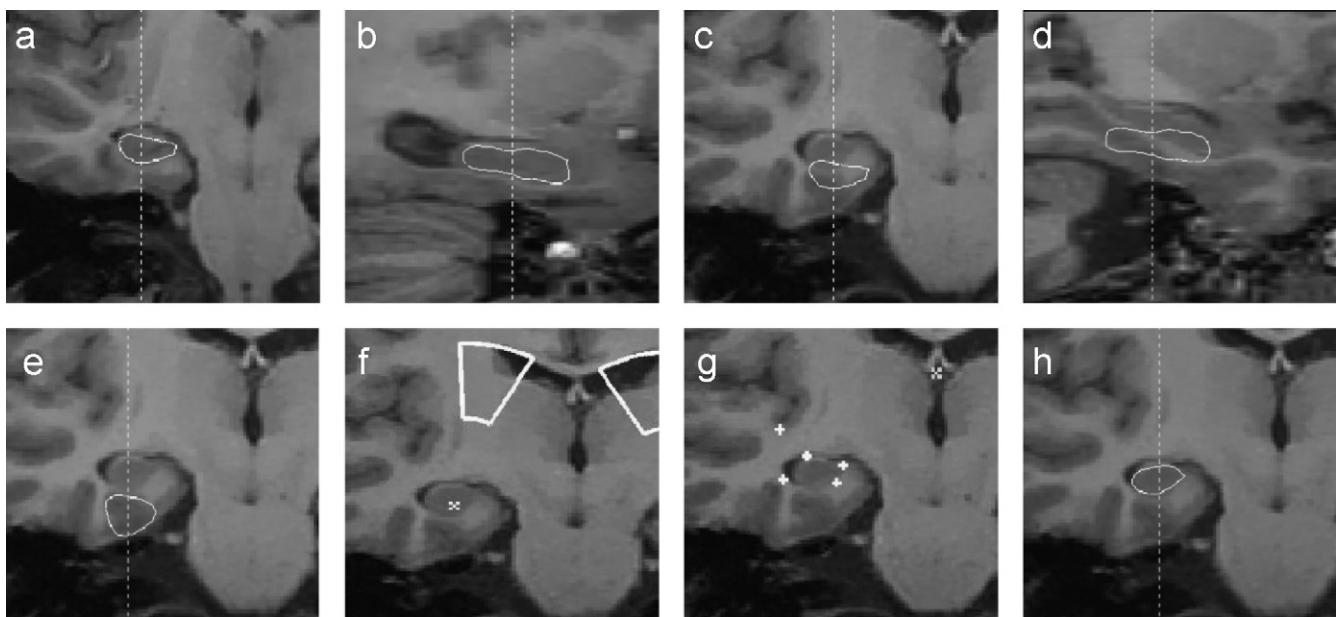
Fig. 14. (a), (b) Coronal and sagittal views of a base MR volumetric data with the hippocampus boundaries overlaid. (c), (d) Hippocampus boundaries transferred from the base to a new MRI data set using mutual information registration. (e) Coronal view of segmented model produced by deformable model using initial model shown in (c) and (d): note an absolute failure: (f) A superior point of the hippocampus transferred model is used to search for the lateral ventricles based on statistical models estimated in Section 2.1 (g) Landmarks of interest found by initialization method. (h) Result of deformable model applied on landmarks shown in (g).

As discussed in Introduction an atlas mapping approach may generate inaccurate initial polygon and have the deformable model fail. Here, we examine an atlas-based initialization approach using a mutual information routine for registration. Then we combine the proposed localization method into the atlas to guide it to the accurate hippocampus location. The atlas mapping leads to a rough localization of the desired structure. However, within that ballpark there is no way to determine the correlation between the landmarks on the boundaries of the mapped model (atlas) and the landmarks in the target image

space. For instance, we do not have any clue as to whether or not the superior landmark of the hippocampus model has been mapped above or below its actual superior landmark. If a deformable model is applied using this initial model, it may be absorbed by the edges of the neighboring structures. However, since we are in close proximity of the structure of interest (hippocampus) we know how to find the previous milestones from which we can search for the actual landmark. In this case, the previous landmark is the lateral ventricles. So we search back for the lateral ventricles in the new image space from

a superior landmark of the hippocampus identified by the atlas. The following paragraph explains our experiment in this regard.

We segment the hippocampus on MR images of one patient shown in coronal and sagittal views, respectively, in Fig. 14(a)–(b). We use the segmented model and the corresponding MRI data set as the atlas that should be mapped to the new patient's MRI. The mutual information is used to register the atlas into the target MRI. Using the registration information, the hippocampus model is then transferred into the new image space (shown in Fig. 14(c)–(d)). Since the hippocampus is not accurately located in the new image space, the result of applying the deformable model provides incorrect results (Fig. 14(e)). The boundaries of the initial model are absorbed by the PFGI, which is a neighbor of the hippocampus with similar features.

We apply the proposed localization method to guide the atlas and correct the hippocampus initialization. Although we do not know where the atlas model falls in the new image space, we know that it is within a close vicinity of the actual hippocampus. Therefore, the structures relatively far from the hippocampus area, e.g., lateral ventricles, should still have the same statistical distributions. We pick a superior point of the transferred hippocampus and perform a search from a viewpoint, 10.9 mm above and 0.78 mm medial to the superior point, to find the right lateral ventricle (Fig. 14(f)). The search area is defined by $\theta_1 = 60.8°$, $\theta_2 = 92°$, $r_1 = 10$, $r_1 = 35$. This is a symmetric counterpart of the search area of the superior landmark of the hippocampus from the lateral points of the lateral ventricles. Then we follow our regular roadmap to find the landmarks of the hippocampus. The result of applying this step is shown in Fig. 14(g). We finally apply the deformable model on the modified initial model to segment the hippocampus (Fig. 14(h)).

4. Conclusions and future work

In this paper we have proposed a novel method to localize the human brain anatomical structures within the MR image space. To evaluate this method, we have applied it to the hippocampus localization problem. The results of this experiment shows that the proposed method is very well capable of landmark initialization and structure identification for small structures with high variability in their shapes and location. This is an important feature that, to the best of our knowledge, no other method is capable of. Landmark identification is important as it provides: (1) initial and intra-procedure information for registration (2) fast navigational guidance through the image data in a highly populated database; (3) initial model for the deformable model segmentation, and (4) valuable (though rough) real time information about the organs and structures of interest.

The proposed method is very focused on the task as it only deals with a few landmarks of interest; therefore, it is very fast. This method emulates the way human experts find an anatomical structure. That is unlike atlas-based methods no expert looks through the entire data set to localize and segment a structure.

Rather, they look for some landmarks of interest that lead to the structure of interest. They may also verify the identified structure by some well-defined and high-contrast neighboring structures. We compared the speed of the proposed algorithm (with almost perfect results) to a mutual information-based rigid-body registration method (with poor results). It turned out to be 2 s vs. 20 min, which is 600 times faster. The very short execution time of the proposed method makes it suitable for intra-operative procedures as well as content-based image navigation, retrieval and mining in largely populated image databases.

The proposed initialization method can be easily combined with the digital atlases to provide them with anatomical landmarks used in registration and also guide them as we have presented an example in previous section. As a future work, the effects of noise and voxel size on performance of the proposed method can be investigated theoretically followed by simulation and real situation studies. Such studies will evaluate the robustness of the proposed method to changes in the voxel size and signal-to-noise ratio.

The proposed method may require normalization of brain sizes when applying on non-adult patients or patients with extreme brain sizes (very small or very large). Such normalization can be automatically carried out using the well-known principal component analysis (PCA) method to estimate the parameters of an affine transformation. The proposed coordinate system built upon the starting point of the roadmap can be used in the estimation of this affine transformation. Such scheme can be performed very quickly and it maintains the high-speed advantage of the proposed method. This normalization step can be applied to all patients regardless of their brain size or age group. We anticipate getting higher success rates if such normalization preprocessing is included in the localization process because it reduces the deviations of the landmarks of interest. Note that the inverse transformation matrix will be applied to restore the initial polygon in the native image space. Therefore, the segmentation and volumetry will be carried out in the native image space of each patient without any distortion from the scaling processes.

Abnormal tissues may cause the proposed method to fail as they may generate fake targets for search algorithm or move the normal structures dramatically and change their symmetric appearance that might trouble symmetric rules. However, note that this is also a problem for the methods that are based on atlas warping. As a future work we will reduce the sensitivity of the method to the presence of abnormal tissues. The symmetric rules do also suffer when there is a tendency towards the sagittal direction on scanned slices. In such case MRI volume should be resliced.

In this work we have used linear combinations of a set of variables for generating the binary images and calculating the CNF. The proposed coefficients were found experimentally and they are not necessarily optimal. Linear discriminant analysis or LASSO (least absolute shrinkage and selection operator) techniques combined with bootstrapping strategies can be used to automatically find the optimal coefficients. The proposed information analysis scheme, which can be considered as an ex-

tension of the conventional rule-based systems, did its job very impressively in our application. However, there are other information analysis methods one may choose from, e.g., Bayesian networks and plausibility measures and calculus. It would be a future work to see how the other information analysis schemes perform in localizing and identifying the hippocampus and other human brain structures.

5. Summary

We present a knowledge-based, fully automatic and very fast method to localize small and highly variable brain structures (e.g., hippocampus) on MR images. Localization procedure consists of two steps: information extraction and analysis. As a prerequisite, information extraction generates binary images of CSF, gray matter, and white matter using FCM clustering. On these binary images, landmarks of lateral ventricles, hippocampus and insular cortex are searched for. Search areas are determined using desired and undesired statistical distributions, which are estimated through expert manual landmark identification on a training set consisting of six epileptic patients. Undesired landmarks are points close to desired landmarks with similar features that can mislead search procedure. A search algorithm examines each search area in a specific order to find a point with a particular color and neighboring connectivity. At information analysis step, a rule-based system evaluates reliability and accuracy of points that are found during information extraction step. Three types of rules are proposed; (1) absolute spatial; (2) relative spatial, and (3) symmetric. A linear combination of uncertain results produced by proposed rules determines an overall confidence factor (CNF). For each slice, CNF determines the likelihood of presence of hippocampus and the accuracy of its landmarks. Finally, a triangulation method followed by a 3D deformable surface model produces the segmentation of the hippocampus. In its application to 10 randomly selected epileptic patients, the proposed method correctly identified all slices without hippocampus. Total success rate for hippocampus localization was 83% and average similarity between manual and automatic segmentations was 0.63 where similarity is defined as intersection of two regions over their union.

Acknowledgment

Appendix A.

Details of the parameters estimation for the roadmaps to localize hippocampus are presented in this Appendix.

A.1. Statistical model and search areas for lateral ventricles

The viewpoint of the search for the lateral ventricles (starting point of the roadmap) is a point on the brain midplane inferior to the most superior limits of the head by half of the head width.

Fig. 15(a) shows the CSF binary image on which the skull is also shown where three lines at the superior and the lateral limits of the head have been drawn. These three lines determine the width and the most superior limits of the head providing the coordinates of the starting point of the search (point-1 in Fig. 15(b)). The desired landmarks are the left and right lateral ventricles each marked by 3 points (point-2 in Fig. 15(b)). The undesired landmarks are illustrated in Fig. 15(a) (point-3, point-4, point-5, and point-6). The distribution of the desired and undesired points for about 50 images of the training set patients are shown and the iso-contours (at 95% confidence level) and the search areas are schematically depicted in Fig. 15(c). The search angles and radii along with the limiting lines are summarized in Table 4. When a point colored black is found, we employ the FCC algorithm with the structuring element shown in Fig. 8(a) to segment the whole structure connected to the found point as the left/right lateral ventricle. Then we find the superior, inferior, lateral, and medial landmarks of the segmented structure that are used later in the information analysis section.

A.2. Statistical model and search area for superior landmarks of hippocampus

The searches for the superior landmarks of the hippocampi (Fig. 16(a) point-4) are initiated from the lateral points of the lateral ventricles (Fig. 16(a) point-1). The undesired landmarks are illustrated in Fig. 16(a) (point-2, point-3). The desired and undesired structures are marked on over 60 slices of images of the training set. The marked points and the iso-contours (at 95% confidence level) derived from the marked points are shown in Fig. 16(b). Using the method to find an optimal viewpoint, discussed in 2.1.3, the point referred to by the arrow shown in Fig. 16(b) is found. This point is reached from the lateral limits of the left lateral ventricle by a translation of $(-1, -14)$. A similar point is determined for the right brain hemisphere. We search for a black point with at least 5 black neighbors in its 8-nearest neighborhood on GM binary images. The search angles and radii are given in Table 4.

A.3. Statistical model and search area for medial inferior limits of insular cortex

The search for the medial inferior landmark of the insular cortex (Fig. 17(a) point-2) is initiated from the superior points of the hippocampus (Fig. 17(a) point-4). The undesired landmarks are illustrated in Fig. 17(a) (point-1, point-3). The search angles and radii along with the limiting lines are summarized in Table 4. Note that the limiting lines (as well as the search areas) are defined in two different coordinate systems, i.e., the coordinate systems of left and right superior landmarks of hippocampus. Fig. 17(b) illustrates the search performed for the left side. The search is for a black point with at least 6 black neighbors in its 8-nearest neighborhood on GM binary images. When a point of the insular cortex is found, we extend its connected region downward to find the inferior landmark of
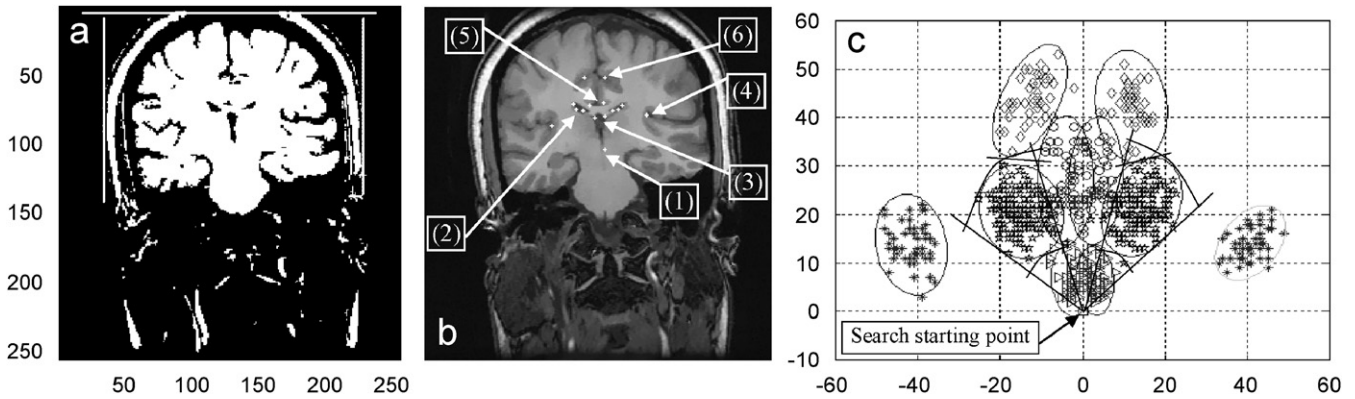
Fig. 15. (a) BK&CSF binary image on which lateral and superior limits of head are determined to find starting point of search. (b) Manual landmark identification for lateral ventricles when looking from starting point (point-1); lateral ventricles (point-2) as desired landmark, top corners of third ventricle (point-3), Sylvian fissure (point-4), and lateral points of callosal sulcus (point-5) and eingulate sulcus (point-6) as undesired landmarks. (c) Distribution of desired and undesired landmark points with iso-contours drawn at 95% confidence level.

Table 4
Summary of each segment (search area) of roadmap estimated based on proposed supervised procedure

View point	Target point	θ_1	θ_2	r_1 (mm)	r_2 (mm)	Limiting line
Starting point	Left lateral ventricle	36.9°	72.9°	29.6	11.7	$y = 0.283x + 21.1$
Starting point	Right lateral ventricle	148°	108.4°	29.6	11.7	$y = -0.283x + 21.1$
Left lateral ventricle	Left superior hippocampus	−30.9°	−92°	7.8	27.3	–
Right lateral ventricle	Right superior hippocampus	−149.2°	−88°	7.8	27.3	–
Left superior hippocampus	Left insular cortex	14.9°	111.3°	6.2	25	$y = 1.195x + 20.3$
Right superior hippocampus	Right insular cortex	76.5°	165.1°	6.2	25	$y = -1.195x + 20.3$
Left insular cortex	Left lateral hippocampus	−163.8°	−66.8°	3.9	15.6	–
Right insular cortex	Right lateral hippocampus	−16.2°	−71.6°	3.9	15.6	–
Left superior hippocampus	Left inferior hippocampus	−48.37°	−108.44	2	13.7	$y = \pm(0.584)x - 14$
Right superior hippocampus	Right inferior hippocampus	−63.95°	−120.96°	2	13.7	$y = \pm(2.250)x - 25$
Left superior hippocampus	Left fourth point	See the text		6.2	25	–
Right superior hippocampus	Right fourth point	See the text		6.2	25	–

this structure using FCC with the structuring element shown in Fig. 8(b). Fig. 17(c) illustrates an instance of the grown region.

A.4. Statistical model and search area for lateral landmarks of hippocampus

We perform a search from the medial inferior landmarks of the insular cortex (Fig. 18(a) point-1) for the lateral landmarks of the hippocampus (Fig. 18(a) point-2) as the desired points. The undesired landmarks are illustrated in Fig. 18(a) (point-3, point-4). The search is performed for a black point with at least 3 black neighbors in its 4-nearest neighborhood on GM binary images. The search angles and radii are given in Table 4.

A.5. Statistical model and search area for inferior landmarks of hippocampus and search for fourth point of hippocampus

As mentioned, the hippocampus looks like a peninsula of gray matter extended horizontally in white matter on the coronal T1-weighted MR images. To find the inferior landmarks of the hippocampus (Fig. 18(b) point-1) a search is initiated from the superior point of this structure (Fig. 18(b) point-2). The undesired landmarks are illustrated in Fig. 18(b) (point-3, point-4). The models derived from the marked points are shown in Fig. 18(c) with the iso-contours drawn at 95% confidence level. The search is performed for a black point with at least 7 black neighbors in its 8-nearest neighborhood on WM binary images. The search angles and radii along with the limiting
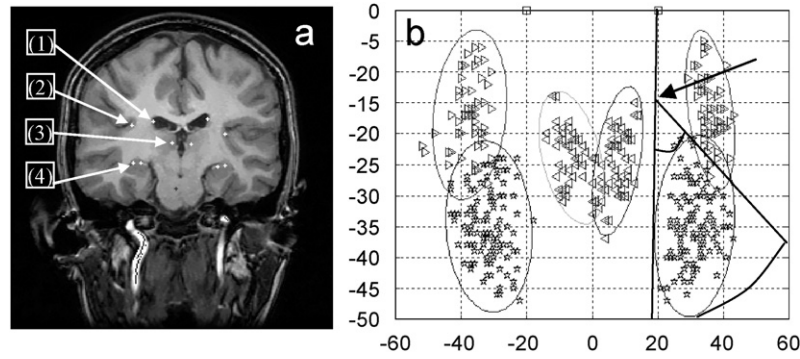
Fig. 16. (a) Manual landmark identification for desired and undesired structures when looking for superior points of hippocampus from lateral points of lateral ventricles (point-1). Medial limits of insular cortex (point-2) and lateral inferior limits of hypothalamus (point-3) are undesired landmarks, and superior point of hippocampus (point-4) is desired landmarks. (b) Manually marked desired and undesired landmarks with iso-contours at 95% confidence level. Search area for left hemisphere is depicted. Note that viewpoint is moved to an optimal position (marked by an arrow on (b)) to balance sensitivity and specificity.
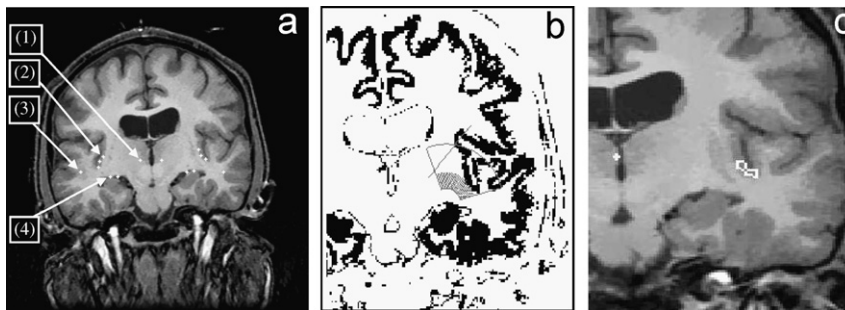

Fig. 17. (a) Manual landmark identification for desired and undesired structures when looking from superior points of hippocampus (point-4). Medial point of insular cortex (point-2) is desired point. Lateral limits of hypothalamus (point-1) and medial limits of SMGTI (point-3) are undesired landmarks. (b) Search performed on a GM binary image to find a black point with at least 6 neighboring black points in its 8-nearest neighborhood. (c) Region connected to point found in (b) is grown downward by applying FCC.
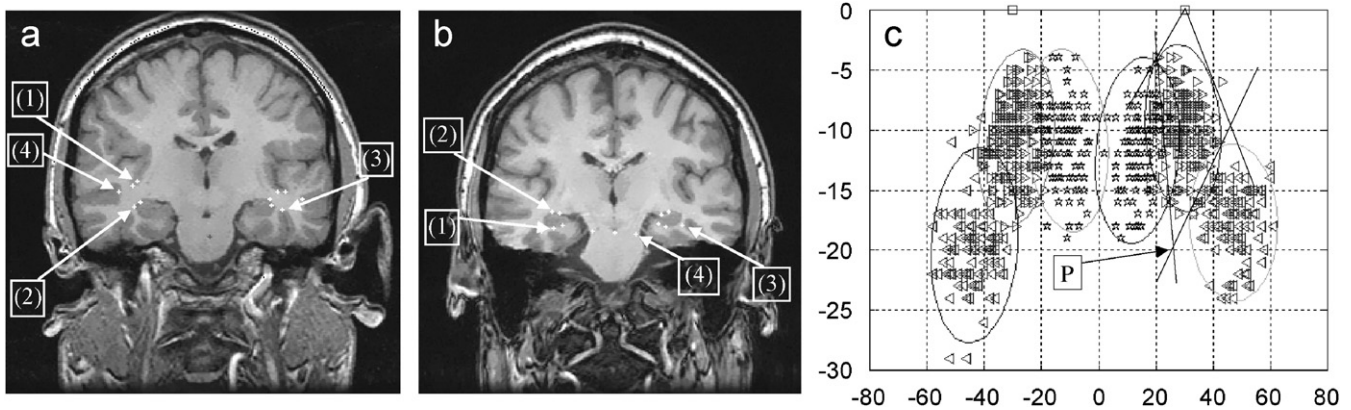
Fig. 18. (a) Manual landmark identification for desired and undesired structures when looking from medial inferior point of insular cortex (point-1) for lateral points of hippocampus (point-2) as desired landmarks. Medial limits of SMGTI (point-4), and superior limits of PFGI (point-3) are undesired landmarks. (b) Manual landmark identification when looking for inferior point of hippocampus (point-1) as desired landmark from superior point of this structure (point-2). Lateral limits of PFGI (point-3), and lateral boundaries of peduncular (point-4) are marked as undesired landmarks. (c) Distribution of desired and undesired landmarks with iso-contour drawn at 95% confidence level for landmarks marked on (b). Arrow and letter "P" mark optimal viewpoint.

lines are summarized in Table 4. The iso-contours shown in Fig. 18(c) suggest to move the viewpoint to the location marked as "P." However, since this is a radical change for the viewpoint as we discussed it in Section 2.1.3, the original viewpoint is used.

For the fourth point of the hippocampus, we compute the median bisector of the edge connecting the inferior and the lateral points of the hippocampus in a triangle formed by these two points and the superior point of the hippocampus. We search from the superior point of the hippocampus in the direction of

the median bisector with $\pm 2°$ deviations. The search is performed for a black point with at least 2 black neighbors in its 4-nearest neighborhood and the search radii are given in Table 4.

References

[1] C.R. Jack, R.C. Petersen, P.C. O'Brien, E.G. Tangalos, MR-based hippocampal volumetry in the diagnosis of Alzheimer's disease, Neurology 42 (1) (1992) 183–188.

[2] F. Cendes, F. Andermann, P. Gloor, A. Evans, M. Jones-Gotman, C. Watson, D. Melanson, A. Olivier, T. Peters, I. Lopes-Cendes, et al., MRI volumetric measurement of amygdala and hippocampus in temporal lobe epilepsy, Neurology 43 (4) (1993) 719–725.

[3] Y.Y. Hsu, N. Schuff, D.L. Amend, A.T. Du, D. Norman, H.C. Chui, W.J. Jagust, M.W. Weiner, Quantitative magnetic resonance imaging differences between Alzheimer disease with and without subcortical lacunes, Alzheimer Dis. Assoc. Disord. 16 (2) (2002) 58–64.

[4] G.B. Frisoni, C. Testa, A. Zorzan, F. Sabattoli, A. Beltramello, H. Soininen, M.P. Laakso, Detection of grey matter loss in mild Alzheimer's disease with voxel based morphometry, J. Neurol. Neurosurg. Psychiatry 73 (6) (2002) 657–664.

[5] A.T. Du, N. Schuff, D. Amend, M.P. Laakso, Y.Y. Hsu, W.J. Jagust, K. Yaffe, J.H. Kramer, B. Reed, D. Norman, H.C. Chui, M.W. Weiner, Magnetic resonance imaging of the entorhinal cortex and hippocampus in mild cognitive impairment and Alzheimer's disease, J. Neurol. Neurosurg. Psychiatry 71 (4) (2001) 441–447.

[6] V.A. Cardenas, A.T. Du, D. Hardin, F. Ezekiel, P. Weber, W.J. Jagust, H.C. Chui, N. Schuff, M.W. Weiner, Comparison of methods for measuring longitudinal brain change in cognitive impairment and dementia, Neurobiol. Aging 24 (4) (2003) 537–544.

[7] E.D. Bigler, D.F. Tate, Brain volume, intracranial volume, and dementia, Invest. Radiol. 36 (9) (2001) 539–546.

[8] S. Dupont, M. Ottaviani, L. Thivard, F. Semah, Y. Samson, M. Baulac, Temporal pole hypometabolism may be linked to a reduction of grey matter in temporal lobe epilepsy, Neuroreport 13 (18) (2002) 2537–2541.

[9] J.C. Pruessner, S. Kohler, J. Crane, M. Pruessner, C. Lord, A. Byrne, N. Kabani, D.L. Collins, A.C. Evans, Volumetry of temporopolar, perirhinal, entorhinal and parahippocampal cortex from high-resolution MR images: considering the variability of the collateral sulcus, Cereb. Cortex 12 (12) (2002) 1342–1353.

[10] V.H. Hackert, T. den Heijer, M. Oudkerk, P.J. Koudstaal, A. Hofman, M.M. Breteler, Hippocampal head size associated with verbal memory performance in nondemented elderly, Neuroimage 17 (3) (2002) 1365–1372.

[11] R.C. Gur, F. Gunning-Dixon, W.B. Bilker, R.E. Gur, Sex differences in temporo-limbic and frontal brain volumes of healthy adults, Cereb. Cortex 12 (9) (2002) 998–1003.

[12] G. Villarreal, D.A. Hamilton, H. Petropoulos, I. Driscoll, L.M. Rowland, J.A. Griego, P.W. Kodituwakku, B.L. Hart, R. Escalona, W.M. Brooks, Reduced hippocampal volume and total white matter volume in posttraumatic stress disorder, Biol. Psychiatry 52 (2) (2002) 119–125.

[13] E.D. Bigler, C.V. Anderson, D.D. Blatter, C.V. Andersob, Temporal lobe morphology in normal aging and traumatic brain injury, Am. J. Neuroradiol. (AJNR) 23 (2) (2002) 255–266.

[14] M.D. Kopelman, D. Lasserson, D. Kingsley, F. Bello, C. Rush, N. Stanhope, T. Stevens, G. Goodman, G. Heilpern, B. Kendall, A. Colchester, Structural MRI volumetric analysis in patients with organic amnesia, 2: correlations with anterograde memory and executive tests in 40 patients, J. Neurol. Neurosurg. Psychiatry 71 (1) (2001) 23–28.

[15] E.D. Bigler, C.M. Lowry, C.V. Anderson, S.C. Johnson, J. Terry, M. Steed, Dementia, quantitative neuroimaging, and apolipoprotein E genotype, Am. J. Neuroradiol. (AJNR) 21 (10) (2000) 1857–1868.

[16] R.E. Hogan, K.E. Mark, I. Choudhuri, L. Wang, S. Joshi, M.I. Miller, R.D. Bucholz, Magnetic resonance imaging deformation-based segmentation of the hippocampus in patients with mesial temporal

[17] E.D. Menschik, L.H. Finkel, Neuromodulatory control of hippocampal function: towards a model of Alzheimer's disease, Artif. Intell. Med. 13 (1998) 99–121.

[18] W.W. Lytton, K.M. Hellman, T.P. Sutula, Computer models of hippocampal circuit changes of the kindling model of epilepsy, Artif. Intell. Med. 13 (1998) 81–97.

[19] C.R. Jack, C.K. Twomey, A.R. Zinsmeister, F.W. Sharbrough, R.C. Petersen, G.D. Cascino, Anterior temporal lobes and hippocampal formations: normative volumetric measurements from MR images in young adults, Radiology 172 (2) (1989) 549–554.

[20] C.R. Jack, F.W. Sharbrough, C.K. Twomey, G.D. Cascino, K.A. Hirschorn, W.R. Marsh, A.R. Zinsmeister, B. Scheithauer, Temporal lobe seizures: lateralization with MR volume measurements of the hippocampal formation, Radiology 175 (2) (1990) 423–429.

[21] H.M. Duvernoy, The Human Hippocampus: An Atlas of Applied Anatomy, J.F. Bermann, Munich 1998, pp. 77–91.

[22] C. Watson, F. Andermann, P. Gloor, et al., Anatomic basis of amygdaloid and hippocampal volume measurement by magnetic resonance imaging, Neurology 42 (1992) 1743–1750.

[23] U. Bick, A. Sprinz, J. Weglage, G. Kurlemann, G. Schuierer, P.E. Peters, Computer-assisted MRI-volumetry of the amygdala and hippocampus in healthy young adults with a history of febrile convulsions in childhood, in: H.U. Lemke, K. Inamura, M.W. Vannier (Eds.), Proceedings of the Computer Assisted Radiology and Surgery (CAR'97), Amsterdam, The Netherlands, 1998, pp. 101–104.

[24] F. Ohl, T. Michaelis, H. Fujimori, J. Frahm, S. Rensing, E. Fuchs, Volumetric MRI measurements of the tree shrew hippocampus, J. Neurosc. Methods 88 (2) (1999) 189–193.

[25] G. Bartzokis, L.L. Altshuler, T. Greider, J. Curran, B. Keen, W.J. Dixon, Reliability of medial temporal lobe volume measurements using reformatted 3D images, Psychiatry Res. Neuroimag. Sect. 82 (1998) 11–24.

[26] I. Claude, J-L. Daire, G. Sebag, Fetal brain MRI: segmentation and biometric analysis of the posterior fossa, IEEE Trans. Biomed. Eng. 51 (4) (2004) 617–626.

[27] J. Webb, A. Guimond, P. Eldridge, D. Chadwick, J. Meunier, J.P. Thirion, N. Roberts, Automatic detection of hippocampal atrophy on magnetic resonance images, Magn. Reson. Imag. 17 (8) (1999) 1149–1161.

[28] G.E. Christensen, R.D. Rabbitt, M.I. Miller, 3D brain mapping using a deformable neuroanatomy, Phys. Med. Biol. 39 (1994) 609–618.

[29] G.E. Christensen, R.D. Rabbitt, M.I. Miller, Deformable templates using large deformation kinematics, IEEE Trans. Imag. Proc. 5 (10) (1996) 1435–1447.

[30] M.I. Miller, G.E. Christensen, Y. Amit, et al., Mathematical textbook of deformable neuroanatomies, Proc. Natl. Acad. Sci. USA, Medical Sciences 90 (1993) 11944–11948.

[31] A.C. Evans, W. Dai, L. Collins, et al., Warping of a computerized 3D atlas to match brain image volumes for quantitative neuroanatomical and functional analysis, SPIE 1445 (1991) 236–246.

[32] A. Davatzikos, B.R. Christos, R. Nick, Using a deformable surface to obtain a shape representation of the cortex, IEEE Trans. Med. Imag. 15 (6) (1996) 785–795.

[33] C. Davatzikos, J.L. Prince, Brain image registration based on curve mapping, Proceedings of IEEE Workshop Biomedical Image 1994, Los Alamitos, CA, USA, 1994, pp. 245–254.

[34] B.C. Vemuri, J. Ye, Y. Chen, C.M. Leonard, Image registration via level-set motion: applications to atlas-based segmentation, Med. Image Anal. 7 (1) (2003) 1–20.

[35] Y-Y. Hsu, N. Schuff, A-T. Du, K. Mark, X. Zhu, D. Hardin, M.W. Weiner, Comparison of automated and manual MRI volumetry of hippocampus in normal aging and dementia, J. Magn. Reson. Imag. 16 (2003) 305–310.

[36] B. Fischl, D.H. Salat, E. Busa, M. Albert, M. Dieterich, C. Haselgrove, A. van der Kouwe, R. Killiany, D. Kennedy, S. Klaveness, A. Montillo, N. Makris, B. Rosen, A.M. Dale, Whole brain segmentation: automated labeling of neuroanatomical structures in the human brain, Neuron. 33 (3) (2002) 341–355.

[37] A. Ghanei, H. Soltanian-Zadeh, J.P. Windham, Segmentation of hippocampus from brain MRI using deformable contours, Computer. Med. Imag. Graph. 22 (3) (1998) 203–216.

[38] A. Kelemen, G. Szekely, G. Gerig, Elastic model-based segmentation of 3-D neuro-radiological data sets, IEEE Trans. Med. Imag. 18 (10) (1999) 828–839.

[39] A. Pitiot, A.W. Toga, P.M. Thompson, Adaptive elastic segmentation of brain MRI via shape-model-guided evolutionary programming, IEEE Trans. Med. Imag. 21 (8) (2002) 910–923.

[40] A. Ghanei, H. Soltanian-Zadeh, J.P. Windham, A 3D deformable surface model for segmentation of objects from volumetric data in medical images, Comput. Biol. Med. 28 (3) (1998) 239–253.

[41] B.M. Dawant, S.L. Hartmann, J-P. Thirion, F. Maes, D. Vandermeulen, P. Demaerel, Automatic 3-D segmentation of internal structures of the head in MR images using a combination of similarity and free-form transformations: I. Methodology and validation on normal subjects, IEEE Trans. Med. Imag. 18 (10) (1999) 909–916.

[42] R. Valdes-Cristerna, V. Medina-Banuelos, O. Yanez-Suarez, Coupling of radial-basis network and active contour model for multispectral brain MRI segmentation, IEEE Trans. Biomed. Eng. 51 (3) (2004) 459–470.

[43] D. Shen, S. Moffat, S.M. Resnick, C. Davatzikos, Measuring size and shape of the hippocampus in MR images using a deformable shape model, Neuroimage 15 (2) (2002) 422–434.

[44] J.L. Boes, C.R. Meyer, T.E. Weymouth, Liver definition in CT using a population-based shape model, Lecture Notes in Computer Science, Computer Vision, Virtual Reality and Robotics in Medicine (CVRMed '95), Nice, FR: 1995, pp. 506–512.

[45] J.W. Snell, M.B. Merickel, J.C. Goble, J.B. Brookeman, N.F. Kassell, Model-based segmentation of the brain from 3-D MRI using active surfaces, IEEE Annual Northeast Bioengineering Conference, New Jersey, March 18–19, 1993, pp. 164–165.

[46] J.F. Brinkley, A flexible generic model for automatic shape: application to interactive two-dimensional medical image segmentation and matching, Comput. Biomed. Res. 26 (2) (1993) 121–142.

[47] P.M. Thompson, A.W. Toga, Detection, visualization, and animation of abnormal anatomic structure with a deformable probabilistic brain atlas based on random vector field transformation, Med. Image Anal. 1 (4) (1997) 271–294.

[48] C-H. Chang, A. Rangarajan, G. Gindi, Segmentation using atlas-guided deformable contour, Proc. of SPIE 2353 (1994) 192–203.

[49] E. Fisher, R.M. Cothren, J.A. Tkach, T.J. Masaryk, J.F. Cornhill, Knowledge-based 3D segmentation of the brain in MR images for quantitative multiple sclerosis lesion tracking, SPIE 3034 (PT1-2) (1997) 19–25.

[50] T.T. Yeo, W.L. Nowinski, Functional neurosurgery aided by using of an electronic brain atlas, Acta Neurochir (Suppl), 68 (1997) 93–99.

[51] G.B. Aboutanos, B.M. Dawant, Automatic brain segmentation and validation: image-based versus atlas-based deformation models, SPIE 3034 (PT1-2) (1997) 299–310.

[52] O. Migneco, J. Darcourt, J. Benoliel, et al., Computerized localization of brain structures in single photon computed tomography using a proportional anatomical stereotactic atlas, Comput. Med. Imag. Graph. 18 (6) (1994) 413–422.

[53] R.O. Duda, P.E. Hart, D.G. Stork, Pattern Classification, second ed., Wiley and Sons, Inc., 2001.

[54] P. Arabie, L.J. Hubert, G. De Soete, Clustering and Classification, World Scientific, River Edge, NJ, 1998.

[55] J.T. Tou, R.C. Gonzalez, Pattern Recognition Principles, Addison-Wesley, Reading, MA, 1974.

[56] G.E. Forsythe, M.A. Malcolm, C.B. Moler, Computer Methods for Mathematical Computations, Prentice-Hall, Englewood Cliffs, NJ, 1976.

[57] R.C. Gonzalez, R.E. Woods, Digital Image Processing, second ed., Addison-Wesley, Reading, MA, 2002.

[58] A. Ghanei, H. Soltanian-Zadeh, A discrete curvature-based deformable surface model with application to segmentation of volume images, IEEE Trans. Inform. Technol. Biomed. 6 (4) (2002).

[59] A. Ghanei, H. Soltanian-Zadeh, A. Ratkewicz, F-F. Yin, A three-dimensional deformable model for segmentation of human prostate from ultrasound images, Med. Phys. 28 (10) (2001) 2147–2153.

Mohammad-Reza Siadat, was born in Tehran, Iran in 1970. He received his B.S. degree in electrical engineering: electronics and his M.S. degree in biomedical engineering: bioelectric from Sharif University of Technology and the University of Tehran, both in Tehran, Iran in 1994 and 1997, respectively. In 2005, he received his Ph.D. degree in computer science from Wayne State University, Detroit, Michigan, USA. Since 2005, he has been with the Department of Radiology, Henry Ford Health System, Detroit, Michigan, USA, where he is currently a Research Scientist/Instructor. In 2003 and 2004 he served as a consultant in Computer Assisted Surgery Laboratory, Neurological Surgery Department, Harper Hospital, Detroit Medical Center—Wayne State University Medical School, Detroit, Michigan, USA. Dr. Siadat's research interests include Biomedical Image and Signal Processing, Biomedical Informatics and Computational Biomedicine and Decision Support Systems. He has authored or co-authored over 20 papers in journals and refereed proceedings, and one book chapter.

Hamid Soltanian-Zadeh, was born in Yazd, Iran in 1960. He received B.S. and M.S. degrees in electrical engineering: electronics from the University of Tehran, Tehran, Iran in 1986 and MSE and Ph.D. degrees in electrical engineering: systems and bioelectrical sciences from the University of Michigan, Ann Arbor, Michigan, USA, in 1990 and 1992, respectively. Since 1988, he has been with the Department of Radiology, Henry Ford Health System, Detroit, Michigan, USA, where he is currently a Senior Staff Scientist. Since 1994, he has been with the Department of Electrical and Computer Engineering, the University of Tehran, Tehran, Iran, where he is currently a full Professor, chair of the Biomedical Engineering Group, and director of Control and Intelligent Processing Center of Excellence. Dr. Soltanian-Zadeh has active research collaboration with Wayne State University, Detroit, MI, USA and the Institute for studies in theoretical Physics and Mathematics (IPM), Tehran, Iran. His research interests include medical imaging, signal and image processing and analysis, pattern recognition, and neural networks. He has published over 430 papers in journals and conference records or as book chapters in these areas. He has served on the scientific committees of several international conferences and editorial boards of many scientific journals. He has also served on the study sections of the National Institutes of Health (NIH), National Science Foundation (NSF), American Institute of Biological Sciences (AIBS), and international funding agencies.

Kost V. Elisevich, was Born in 1953 in Sarnia, Ontario, Canada, Kost Elisevich obtained his M.D. (1978) and Ph.D. (Anatomy; 1986) at the University of Western Ontario and completed his training in neurosurgery at McGill University (Montreal Neurological Institute and affiliated hospitals). A fellow of the Royal College of Physicians and Surgeons of Canada and the American College of Surgeons, he is currently a senior staff member of the Department of Neurosurgery at Henry Ford Hospital in Detroit. His current interests include the imaging analysis of focal epilepsy, genomic influences and processes of epileptogenesis. The surgical treatment of epilepsy and the removal of tumors from eloquent cerebral regions remain his primary clinical interests. He has authored over 80 papers and chapters in addition to a book ('Epilepsy Surgery. Case Studies and Commentaries') and serves on the editorial board of Electromagnetics in Biology and Medicine.